Overrepresentation of chromosome 12p sequences and karyotypic evolution in i(12p)-negative testicular germ-cell tumors revealed by fluorescence in situ hybridization, *Cancer Genet. Cytogenet.*, **70**, 85–93.

11. Skotheim, R. I., Monni, O., Mousses, S. et al. 2002, New insights into testicular germ cell tumorigenesis from gene expression profiling, *Cancer Res.*, **62**, 2359–2364.
12. Zafarana, G., Gillis, A. J. M., van Gurp, R. J. H. L. M. et al. 2002, Coamplification of *DAD-R*, *SOX5*, and *EKI1* in human testicular seminomas, with specific overexpression of *DAD-R*, correlates with reduced levels of apoptosis and earlier clinical manifestation, *Cancer Res.*, **62**, 1822–1831.
13. Rodriguez, S., Jafer, O., Goker, H. et al. 2003, Expression profile of genes from 12p in testicular germ cell tumors of adolescents and adults associated with i(12p) and amplification at 12p11.2-p12.1, *Oncogene*, **22**, 1880–1891.
14. Sicinski, P., Donaher, J. L., Geng, Y. et al. 1996, Cyclin D2 is an FSH-responsive gene involved in gonadal cell proliferation and oncogenesis, *Nature*, **384**, 470–474.
15. Houldsworth, J., Reuter, V., Bosl, G. J. et al. 1997, Aberrant expression of cyclin D2 is an early event in human male germ cell tumorigenesis, *Cell Growth Differ.*, **8**, 293–299.
16. Bartkova, J., Meyts, E., Skakkebæk, N. E. et al. 1999, D-type cyclins in adult human testis and testicular cancer: relation to cell type, proliferation, differentiation, and malignancy, *J. Pathol.*, **187**, 573–581.
17. Cipriano, S. C., Chen, L., Burns, K. H. et al. 2001, Inhibin and p27 interact to regulate gonadal tumorigenesis, *Mol. Endocrinol.*, **15**, 985–996.
18. Schmidt, B. A., Rose, A., Steinhoff, C. et al. 2001, Up-regulation of cyclin-dependent kinase 4/cyclin D2 expression but down-regulation of cyclin-dependent kinase 2/cyclin E in testicular germ cell tumors, *Cancer Res.*, **61**, 4214–4221.
19. Shida, K., Terajima, D., Uchino, R. et al. 2003, Hemocytes of *Ciona intestinalis* express multiple genes involved in innate immune host defense, *Biochem. Biophys. Res. Comm.*, **302**, 207–218.
20. Terajima, D., Yamada, S., Uchino, R. et al. 2003, Identification and sequence of seventy-nine new transcripts expressed in hemocytes of *Ciona intestinalis*, three of which may be involved in characteristic cell-cell communication, *DNA Res.*, **10**, 203–212.
21. Wu, L., Timmers, C., Maiti, B. et al. 2001, The E2F1-3 transcription factors are essential for cellular proliferation, *Nature*, **414**, 457–462.
22. Friedmann, Y., Daniel, C. A., Strickland, P. et al. 1994, Hox genes in normal and neoplastic mouse mammary gland, *Cancer Res.*, **54**, 5981–5985.
23. Zhang, X., Zhu, T., Chen, Y. et al. 2003, Human growth hormone-regulated HOXA1 is a human mammary epithelial oncogene, *J. Biol. Chem.*, **278**, 7580–7590.
24. Suzuki, T., Shen, H., Akagi, K. et al. 2002, New genes involved in cancer identified by retroviral tagging, *Nature Genet.*, **32**, 166–174.
25. Okano, M., Bell, D. W., Haber, D. A. et al. 1999, DNA methyltransferases Dnmt3a and Dnmt3b are essential for de novo methylation and mammalian development, *Cell*, **99**, 247–257.
26. Kaneda, M., Okano, M., Hata, K. et al. 2004, Essential role for *de novo* DNA methyltransferase Dnmt3a in paternal and maternal imprinting, *Nature*, **429**, 900–903.
27. Smiraglia, D. J., Szymanska, J., Kraggerud, S. M. et al. 2002, Distinct epigenetic phenotypes in seminomatous and nonseminomatous testicular germ cell tumors, *Oncogene*, **21**, 3909–3916.
28. Okada, K., Katagiri, T., Tsunoda, T. et al. 2003, Analysis of gene-expression profiles in testicular seminomas using a genome-wide cDNA microarray, *Int. J. Oncol.*, **23**, 1615–1635.
29. Sperger, J. M., Chen, X., Draper, J. S. et al. 2003, Gene expression patterns in human embryonic stem cells and human pluripotent germ cell tumors, *Proc. Natl. Acad. Sci. USA*, **100**, 13350–13355.
30. Tusher, V. G., Tibshirani, R., and Chu, G. 2001, Significance analysis of microarrays applied to the ionizing radiation response, *Proc. Natl. Acad. Sci. USA*, **98**, 5116–5121.

DNA RESEARCH 11, 345–352 (2004) Short Communication

Identification of Transcripts Expressed Preferentially in Hemocytes of *Ciona intestinalis* that can be Used as Molecular Markers

Takeshi WAKOH,[1,†] Makoto IKEDA,[1,†] Ryuji UCHINO,[1] Kaoru AZUMI,[2] Masaru NONAKA,[3] Yuji KOHARA,[4] Hitoe METOKI,[5] Yutaka SATOU,[5] Nori SATOH,[5] and Masanobu SATAKE[1,*]

Institute of Development, Aging, and Cancer, Tohoku University, Seiryo-machi, 4-1, Aoba-ku, Sendai 980-8575, Japan,[1] Creative Research Initiative "Sousei," Hokkaido University, 12 Jyou Nishi, 6, Kita-ku, Sapporo 060-0812, Japan,[2] Department of Biological Sciences, Graduate School of Science, University of Tokyo, Hongo 7-3-1, Bunkyo-ku, Tokyo 113-0033, Japan,[3] National Institute of Genetics, Tanita 1111, Mishima 411-8540, Japan,[4] and Department of Zoology, Graduate School of Science, Kyoto University, Kitashirakawa, Oiwake-cho, Sakyo-ku, Kyoto 606-8224, Japan[5]

(Received 5 August 2004; revised 15 September 2004)

Abstract

The immunity provided by ascidian hemocytes represents one prototype of innate immune function in vertebrates. However, there are currently no molecular markers of ascidian hemocytes. We accumulated a large number of ESTs of cDNAs derived from hemocytes of *Ciona intestinalis*, a cosmopolitan species of ascidian. By comparing these ESTs with those derived from other tissues and developmental stages of *Ciona*, we were able to extract 81 transcripts expressed abundantly and preferentially in hemocytes. Among them, the *von Willebrand factor type A (vWA)-like* and *complement 6 (C6)-like* transcripts were found to be expressed almost exclusively in hemocytes, based on RT-PCR analysis and whole mount *in situ* hybridization. We propose that *vWA-like* and *C6-like* can be used as molecular markers for *Ciona* hemocytes.

Key words: ascidian; hemocytes; transcript; molecular marker

Ascidians occupy a unique position in the evolution of deuterostome animals in the sense that a host defense mechanism functioning in ascidians represents a prototype of the innate immunity seen in vertebrates.[1,2] A recent report of the draft genome sequence of *Ciona intestinalis*,[3,4] a cosmopolitan species of ascidians, provided us with the chance to search for and identify the genes responsible for immunity.[2] As expected, genes known to belong to the acquired immunity system, such as the immunoglobulin, T-cell receptor, and RAG genes, were not found; whereas genes known to be involved in innate immunity, such as those for complement and the Toll-like receptors, were detected in the genome. It is particularly interesting that some components resembling the vertebrate's *MHC* genes were detected in a physically linked order in the *Ciona* genome. This favors the idea that ascidians closely precede vertebrates in the evolution of immune function.

Hemocytes are the central players of immunity in ascidians. The cells can phagocytose foreign materials, particularly opsonized ones,[5–7] and can synthesize antimicrobial peptides.[8–11] Using cDNA/EST studies, we recently found that various transcripts related to host defense are expressed in *Ciona* hemocytes.[12,13] However, a lack of molecular probes for hemocytes hampers the rapid progress of ascidian immunology. The number of hemocyte ESTs we reported previously (3,353) is very limited for the purpose of identifying such markers. In the present study, we wanted to see firstly what kind of transcripts are abundantly and preferentially expressed in *Ciona* hemocytes. Then, by using this information, we wanted to identify the molecular markers of *Ciona* hemocytes. To accomplish these two aims, we accumulated a relatively large number of cDNAs/ESTs.

The poly(A)$^+$ RNA fraction was isolated from *Ciona* hemocytes as described previously.[12] Conversion of poly(A)$^+$ RNA to cDNA, construction of a cDNA library and EST sequencing were also performed as described previously.[14] The sequences were registered in the DDBJ DNA database and are also available at our

Communicated by Satoshi Tabata

* To whom correspondence should be addressed. Tel. +81-22-717-8477, Fax. +81-22-717-8482, E-mail: satake@idac.tohoku.ac.jp

† These two authors contributed to the work equally.

Table 1. The number of clusters as classified into functional groups.

Class			number of TCs
(A) Functions that many kinds of cells use			
A I	Transpotation and binding proteins for ions and small molecules		0
A II	RNA processing,polymerizing,splicing and binding proteins,and enzymes		0
A III	Cell replication,histones,cyclins and allied kinases,DNA polymerases,topoisomerases,DNA modification		0
A IV	Cytoskelton and membrane proteins		7
A V	Protein synthesis co-factors,tRNA synthetases,ribosomal proteins		0
A VI	Intermediary synthesis and catabolism enzymes		2
A VII	Stress response,detoxification and cell defense proteins		3
A VIII	Protein degradation and processing,proteases		4
A IX	Transpotation and binding proteins for proteins and other macromolecules		1
		Subtotal	17
(B) Cell-cell communication			
B I	Signaling receptors,including cytokine and hormone receptors,and signaling ligands		3
B II	Intracellular signal transduction pathway molecules including kinases and signal intermediates		5
B III	Extracellular matrix proteins and cell adhesion		5
		Subtotal	13
(C) Transcription factors and other gene regulatory proteins			4
		Subtotal	4
(D) Miscellaneous			
D I	Not enough information to classify		6
D II	Not significant similarities to known proteins		41
		Subtotal	47
		Total	81

Functional classification used here is based on that employed by a series of *Ciona*'s cDNA/EST studies.[12–21] As for the details of each TC, see Table 2.

URL, http://ghost.zool.kyoto-u.ac.jp. In the present study, however, we used Release 2.0 ESTs that are available at the TIGR database at http://www.tigr.org/tigr-scripts/tgi/T_index.cgi?species=c_intestinalis; these ESTs are clustered into tentative consensus sequences (TCs). The hemocyte ESTs collected in this study are seen in the BM7 library (n=56,709, in these, the 5′- and 3′-ESTs represent 28,322 and 28,387, respectively), whereas those in our previous report[12] are in the 9VV library (n=3,353). For the purpose of comparison, we also used *Ciona* ESTs/TCs obtained from other tissues and various developmental stages of *C. intestinalis*.[14–21] The total numbers of *Ciona* ESTs and TCs in the TIGR database are 485,757 and 20,813, respectively.

Firstly, from the 7,940 *Ciona* hemocyte TCs, we extracted the TCs that satisfied both of the following criteria: (1) The TC should contain more than 28 ESTs derived from BM7 and (2) The BM7- and 9VV-derived ESTs in the TC should constitute more than 50% of all the ESTs in the TC. Twenty-eight ESTs constitutes 0.05% of 56,709; therefore, a TC that meets this criterion is considered to represent a transcript that is expressed abundantly in hemocytes. TCs that fulfill the second criterion are considered to represent transcripts that are expressed to a greater degree in hemocytes than in other tissues and developmental stages.

Only 81 of 7,940 TCs fulfilled the above two criteria. We used gene annotations and information about ontology attached to each TC and classified the 81 TCs into several functional groups (Table 1). The functional classifications used here have been previously employed in a series of *Ciona*'s cDNA/EST studies.[12–21] Table 2 describes the details of each TC.

A total of 34 of the annotated TCs belong to classes A (functions that many kinds of cells use), B (cell-cell communication), and C (transcription factors and other gene regulatory proteins). Among these, it is noteworthy that 7 of the TCs encode cytoskeletal proteins (class AIV). These TCs may be related to the high locomotive activity of hemocytes. Two *protein tyrosine phosphatase-like* (TC15785 and TC27235 in class BI) but no *protein tyrosine kinase-like* transcripts were found in the list. Integrin alpha precursor-like (TC25665 in class BIII) is likely a receptor for a complement 3-like molecule in *Ciona*.[22] In addition, the 4 TCs that encode transcription factors include *c-Jun-like* (TC15120), *HMG-box-containing Sox17-like* (TC25149), *Ets-domain containing ESE-3A-like* (TC26559), and *zinc-finger-containing PEM-4-like*

Table 2. Clusters expressed abundantly and preferentially in *Ciona* hemocytes.

Class	Cluster ID	Hemocytes BM7	Hemocytes 9VV	Total EST	Hemocytes /Total	Tentative annotation	ORF	aa number	Domain
AIV	TC14917	200	6	217	95%	weakly similar to gelsolin {Danio rerio}, partial (41%)	+	737	GEL(6)
AIV	TC24287	161	16	294	60%	weakly similar to nonmuscle myosin heavy chain {Gallus gallus}, partial (80%)	+	1613	MYSc-IQ-coiled coil(2)
AIV	TC15032	111	4	161	71%	weakly similar to probable fimbrin [imported] - Arabidopsis thaliana, partial (34%)	+	634	EFh(2)-CH(4)
AIV	TC15214	73	0	109	67%	weakly similar to KIAA0320 {Homo sapiens}, partial (20%)	+	786	ILWEQ
AIV	TC15217	64	0	112	57%	weakly similar to Fascin 2 (Retinal fascin). [Bovine], partial (41%)	+	487	
AIV	TC25869	34	1	59	59%	similar to C. elegans TBA-9 protein (corresponding sequence F40F4.5) {Caenorhabditis elegans}, complete	+	447	
AIV	TC24881	34	2	58	62%	weakly similar to gelsolin {Danio rerio}, partial (63%)	+	708	GEL(6)
AVI	TC15414	77	2	97	81%	similar to L-lactate dehydrogenase {Styela plicata}, partial (92%)	+	341	
AVI	TC14620	57	5	68	91%	ATP synthase alpha-subunit {Ciona intestinalis}, partial (33%)	+	63or64	
AVII	TC14643	161	0	170	95%	weakly similar to complement component C6 {Branchiostoma belcheri}, partial (18%)	+	565	TSP1-ZnF NFX-TSP1-LDLa-MACPF-EGF
AVII	TC25302	148	6	175	88%	weakly similar to complement component C6 {Branchiostoma belcheri}, partial (11%)	+	566	MYSc-IQ-coiled coil-TSP1-ZnF NFX-TSP1-LDLa-MACPF-EGF
AVII	TC26782	31	0	57	54%	weakly similar to flavin-containing monooxygenase {Gorilla gorilla}, partial (25%)	+	357	TM
AVIII	TC14696	192	10	252	80%	transglutiminase {Ciona intestinalis}, complete (100%)	+	766	TGc
AVIII	TC24838	81	6	144	60%	weakly similar to 72 kDa type IV collagenase precursor (EC			
AVIII	TC16352	31	4	52	67%		+	666	CLECT-Tryp SPc
AVIII	TC14698	30	4	39	87%	transglutiminase {Ciona intestinalis}, partial (27%)	+	212	
AIX	TC26244	39	3	72	58%	weakly similar to Sly1 protein - rat, partial (19%)	+	388	
BI	TC15785	34	3	54	69%	similar to vascular endothelial protein tyrosine phosphatase {Mus musculus}, partial (7%)	+	529	TM-PTPc
BI	TC27235	33	4	41	90%	weakly similar to amPTPR4c {Branchiostoma belcheri}, partial (38%)	+	546	PTPc(2)
BI	TC14267	32	3	44	80%		+	513	PTPc(2)
BII	TC14430	186	9	279	70%	weakly similar to coronin {Hemicentrotus pulcherrimus}, partial (42%)	+	463	WD40(4)-coiled coil
BII	TC14655	106	5	216	51%	homologue to calmodulin {Metridium senile}, complete (100%)	+	149	EFh(4)
BII	TC25991	54	6	102	59%	weakly similar to putative growth regulator 14-3-3 {Echinococcus granulosus}, partial (93%)	+	263	14 3 3
BII	TC26092	42	0	77	55%	weakly similar to Ras GTPase-activating-like protein IQGAP1 (P195). [Human], partial (42%)	+	928	IQ(4)-coiled coil-Ras GAP-coiled coil(2)
BII	TC27312	37	0	43	86%	weakly similar to Raichu404X {Homo sapiens}, partial (24%)			
BIII	TC24677	409	29	467	94%	weakly similar to Vwa1 protein {Boltenia villosa}, partial (29%)	+	1326	CCP(15)-vwa
BIII	TC25663	90	6	112	86%		+	813	Int alpha(3)-TM
BIII	TC26682	48	2	57	88%	weakly similar to Ci-META1 {Ciona intestinalis}, partial (13%)	+	659	TSP1-EGF-EGF CA-PTI-EGF CA(3)-PTI-EGF CA-ZnF NFX- EGF CA(5)-PTI-EGF CA(2)-TM
BIII	TC25600	41	2	71	61%	weakly similar to integrin beta-3 subunit - African clawed frog, partial (36%)	+	840	PSI-INB-VWA-EGF-TM
BIII	TC25665	29	0	29	100%	weakly similar to integrin alpha Hr1 precursor {Halocynthia roretzi}, partial (13%)	+	1250	VWA-Int alpha(4)-TM
C	TC15120	81	6	140	62%	similar to c-Jun protein {Xenopus laevis}, partial (30%)	+	381	BRLZ
C	TC25149	54	4	75	77%	weakly similar to HMG-box transcription factor Sox17 {Danio rerio}, partial (21%)	+	796	HMG
C	TC26559	44	2	58	79%	weakly similar to transcription factor ESE-3A {Homo sapiens}, partial (35%)	+	552	ETS
C	TC15716	38	2	77	52%	similar to PEM-4 {Ciona savignyi}, partial (20%)	+	599	ZnF C2H2-ZnF NFX-ZnF C2H2(2)
DI	TC15029	108	3	167	66%	Not2 {Ciona intestinalis}, complete (100%)	+	412	SERPIN
DI	TC26106	70	2	84	86%	weakly similar to hypothetical protein CL25084 {Homo sapiens}, partial (27%)	+	453	coiled coil
DI	TC24275	65	20	163	52%	homologue to Ci-META4 {Ciona intestinalis}, partial (97%)	+	103	TM
DI	TC15881	34	2	68	53%	weakly similar to FLJ00024 protein {Homo sapiens}, partial (68%)	+	967	

Table 2. Continued.

Class	Cluster ID	Hemocytes BM7	Hemocytes 9VV	Total EST	Hemocytes /Total	Tentative annotation	ORF	aa number	Domain
DI	TC24361	33	0	50	66%	weakly similar to FLJ00240 protein {Homo sapiens}, partial (59%)	-	1290	LRR RI(6)-coiled coil(2)
DI	TC26489	32	1	51	65%	weakly similar to Hypothetical protein C04D8.1 {Caenorhabditis elegans}, partial (11%)	+	309	Rho GAP
DII	TC24415	299	13	402	78%		+	268	
DII	TC25212	239	8	417	59%		+	123	ZnF NFX
DII	TC15080	106	4	129	85%		+	487	TM-TEP1(3)-EGF-TSP1(2)-EGF
DII	TC14925	102	5	213	50%		+	204	CH
DII	TC15163	100	6	135	79%		+	337	NEBU(3)
DII	TC25608	92	0	141	65%		+	317	TM(4)
DII	TC25643	87	2	155	57%		+	341	TM
DII	TC25166	84	0	95	88%		+	154	TM
DII	TC25165	71	0	77	92%		+	175	TM
DII	TC14720	70	18	130	68%		+	62	TM
DII	TC25213	67	4	92	77%		+	336	coiled coil-TM
DII	TC15215	66	2	125	54%		+	755	CUB(6)
DII	TC15558	62	1	89	71%		+	317	CUB-ZnF NFX
DII	TC25599	49	0	87	56%		+	52	TM
DII	TC25556	49	6	56	98%		-	427	TSP1(5)-ZnF NFX- TSP1(3)
DII	TC26265	47	0	72	65%		+	403	ZP-EGF-TM
DII	TC16155	45	6	59	86%		+	219	TM(4)
DII	TC15992	43	2	65	69%		+	490	JmjC
DII	TC25911	41	0	67	61%		+	146	
DII	TC26361	41	1	55	76%		+	447	SH2
DII	TC15653	40	2	82	51%		+	366	TM(7)
DII	TC25209	40	2	50	84%		+	581	TM(7)
DII	TC26388	40	4	73	60%		+	137	ZnF NFX
DII	TC27213	37	2	45	87%		+	176	TM
DII	TC16675	36	0	44	82%		+	159	
DII	TC26594	35	0	62	56%		+	439	CUB(2)-TM
DII	TC26530	35	0	41	85%		+	158	
DII	TC15312	34	0	41	83%		+	529	TM(7)
DII	TC16853	34	0	40	85%		+	107	TM
DII	TC24905	33	0	47	70%		+	657	ZnMc-ShKT(2)
DII	TC27089	32	2	42	81%		+	647	
DII	TC16049	32	2	36	94%		+	281	LRR TYP(3)
DII	TC16116	32	0	55	58%		+	411	PH
DII	TC25623	31	0	45	69%		+	376	
DII	TC27323	31	3	37	92%		+	560	EGF CA-VWA-EGF CA(3)-VWA
DII	TC24906	30	0	51	59%		+	151	coiled coil
DII	TC25587	30	3	58	57%		+	566	TM(2)
DII	TC16421	30	0	33	91%		+	501	JmjC
DII	TC16408	29	4	49	67%		+	366	TM(5)
DII	TC26927	29	3	49	65%		+	352	
DII	TC26587	28	4	57	56%		+	378	Rho GEF-PH

See the main text as for the numbers and the percentages of ESTs that constitute each TC cluster. Briefly, the sources of ESTs are from hemocytes (BM7 and 9VV) or others and "Total" represents the sum of hemocytes- and others-derived ESTs. Contribution of hemocytes' ESTs to the total ESTs in each TC is indicated as the percentage. Tentative annotation represents the gene to which each TC cluster showed the highest homology by the BLAST program[24] and the percentage of identical amino acid residues between the two genes is shown in parenthesis. TC16352, TC14267 and TC25663 are classified as AVIII, BI and BIII, respectively, based on their domain architecture, although they did not show any significant homology to known genes. The number of amino acid residues in the polypeptide encoded by the open reading frame (ORF) is presented. Minus of ORF means the lack of initiating methionine codon in the encoded polypeptide. The feature and number of domains identified by the SMART program[25] is also shown.

(TC15716). These transcription factors may play a role in the development, differentiation, and immune function of hemocytes. Non-annotated, 47 TCs belonged to class D (miscellaneous).

Secondly, we selected two genes from the TCs in Table 2, *von Willebrand factor type A (vWA)-like* (TC24677) and *complement 6 (C6)-like* (TC14643), to see whether they could be used as molecular markers of *Ciona* hemocytes. We chose these two TCs because each has a large number of hemocyte-derived ESTs (438 for *vWA* and 161 for *C6*) and each represents a high proportion of the hemocyte contribution to the total ESTs (94% for *vWA* and 95% for *C6*). In addition, as shown in Fig. 1A, domain analysis of the encoded polypeptides revealed that *vWA-like* and *C6-like* each possess characteristic features, the vWA and membrane-attack complex/perforin (MAC/PF) domains, which are unique to mammalian blood coagulation protein and complement,

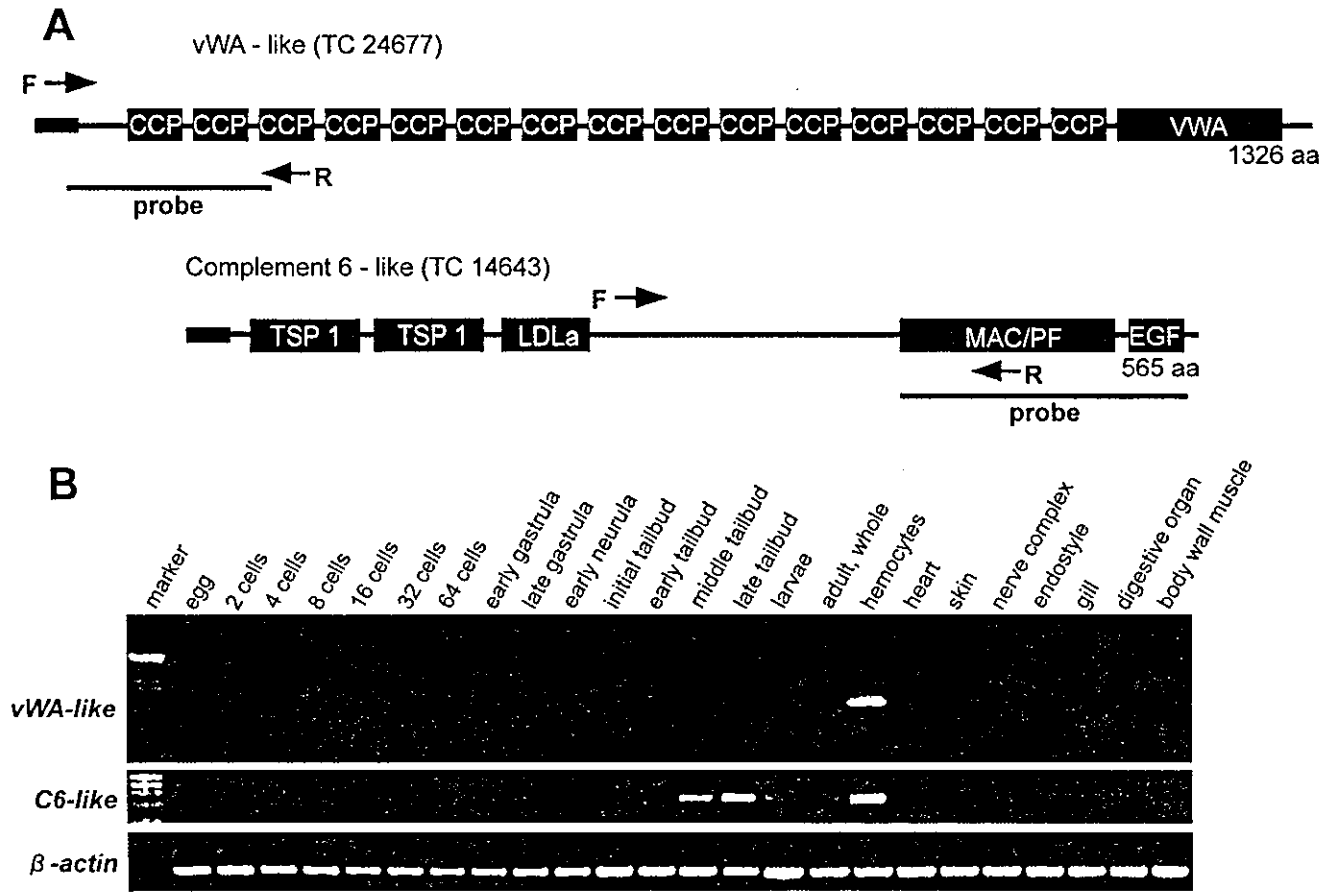

Figure 1. Expression of *vWA-like* and *C6-like* transcripts. (A) Domain analysis of the vWA-like and C6-like polypeptides, which are encoded by TC24677 and TC14643, respectively. Numbers represent amino acid residues. The locations of forward (F) and reverse (R) primers and hybridization probes are indicated. The primers were used in RT-PCR, whereas the probes were used in WISH. CCP, complement control protein modules; vWA, von Willebrand factor type A domain; TSP1, thrombospondin type1; LDLa, low density lipoprotein receptor domain class A; MAC/PF, membrane-attack complex/perforin; EGF, epidermal growth factor receptor. (B) RT-PCR analysis of *vWA-like* and *C6-like* transcripts. RNA was prepared from *C. intestinalis* at various stages of development and from various tissues of 3-month-old adult individuals. These included fertilized eggs, 2-cell embryos, 4-cell embryos, 8-cell embryos, 16-cell embryos, 32-cell embryos, 64-cell embryos, early gastrula, late gastrula, early neurula, immediate early tailbud, early tailbud, mid tailbud, late tailbud, larvae, and 3-month-old whole individuals, hemocytes, heart, skin, nerve complex, endostyle, gills, digestive organ, and body wall muscles. RNA was converted to cDNA by SuperScript II reverse transcriptase (Invitrogen) and a fixed amount of cDNA was used for RT-PCR analysis. The forward and reverse primers were as follows: for *vWA-like*, 5′-ACGGTCTAAAATGTTGGGTGTGCGAC-3′ and 5′-TCCAATCAAAGAAAATCCGGGCGCG-3′, for *C6-like*, 5′-GTTACACTGTGAGGAGTGGTGAAC-3′ and 5′-CCGCCTACTACGTTTGAAATAACT-3′, and for *beta-actin*, 5′-GTGCTTTCATTGTACGCTTCTGGTC-3′ and 5′-CGGCGATTCCAGGGAACATAG-3′. One cycle of PCR was carried out for 60 sec at 94°C, for 30 sec at 60°C, and for 60 sec at 72°C serially, and this cycle was repeated 35 times, using each set of primers and ExTaq (Takara). The amplified products from *vWA-like*, *C6-like*, and *beta-actin* cDNAs were run through agarose gels together with a DNA molecular weight marker.

respectively.

Expression of the *vWA-like* and *C6-like* transcripts was examined with RT-PCR analysis, using RNAs that were prepared from various tissues of 3-month-old adult individuals and from various stages of development. As shown in Fig. 1B, the *vWA-like* transcript was detected only in hemocytes, whereas the *C6-like* transcript was detected mainly, but not exclusively, in hemocytes. Expression of *C6-like* was detected to a lesser degree in tailbud and larva but not in the other tissues or developmental stages. The *beta-actin* transcript was used as a control and was detected throughout development.

We next performed whole mount *in situ* hybridization (WISH) of the *vWA-like* and *C6-like* transcripts, using 3-week-old specimens (Fig. 2). The antisense probes of both *vWA-like* (panels A and B) and *C6-like* (panels E and F) revealed similar multiple dot staining. The blood vessels in the field appeared as transverse and longitudinal bars but the vessels themselves were not stained. To observe more closely what kind of cells were stained, the stained specimens were viewed at a higher magnification. The floating, round cells inside the vessels were positive

Figure 2. WISH of *vWA-like* and *C6-like* transcripts. Three-week-old adult specimens were collected after 5 days of starvation, relaxed with L-menthol, fixed in a solution containing 4% (w/v) paraformaldehyde, 0.5 M NaCl, and 0.1 M MOPS at 4°C for 12 hr, and stored in 80% ethanol at −25°C until use. For WISH, the methods were based on a published protocol.[26] To prepare the RNA probes, the cDNAs inserted into the pBluescript SKII or p-GEM-T vectors were linearized with an appropriate restriction enzyme and used as a template. The reaction was done in a digoxigenin RNA labeling mixture (Roche), using T7 and T3 (or SP6) RNA polymerases to make antisense and sense RNA probes, respectively. The cDNA sequences were derived from the clone ciad046b20 in the case of *C6-like* and the RT-PCR product in the case of *vWA-like*. The RNA probes used were *vWA-like* antisense (A, B and C), *vWA-like* sense (D), *C6-like* antisense (E, F, G and H), and *C6-like* sense (I). The scale bars in A and E are 0.5 mm. The magnifications of the objective lenses used for the microscopic observation were as follows: ×10 for D, F and I; ×20 for B and G; ×40 for C and H. In panel C, the cells indicated by the arrows and arrowheads represent the positively stained and unstained cells, respectively.

for either *vWA-like* (panel C) or *C6-like* (panels G and H). It must be noted, however, that not all of the floating cells were stained by the *vWA-like* probe, and that some cells were certainly not stained (see the stained cells indicated by arrows and the unstained cells indicated by arrowheads in panel C). Probably, *Ciona* hemocytes are not a uniform population but rather consist of functionally heterogeneous cell types, as in the case of *Halocynthia roretzi*.[23] In contrast, the *C6-like* probe stained most of the cells inside the vessels (panels G and H). As controls, the sense probes of *vWA-like* (panel D) and *C6-like* (panel I) did not produce any positive staining. Thus, based on the results of Figs. 1 and 2 together, *vWA-like* and *C6-like* were considered to be useful as markers of hemocytes.

It must be noted that not all of the TCs listed in the tables were good candidates as molecular markers of *Ciona* hemocytes. For example, RT-PCR analysis revealed that each of TC14917 and TC25665, in which the contribution of hemocyte ESTs was more than 95%, was more or less detected in various tissues. On the other hand, another *C6-like* transcript, TC25302, was detected mainly in hemocytes by RT-PCR as well as WISH analysis (data not shown). Therefore, the number of ESTs accumulated in the present study appears not to be sufficient to extract conclusively the marker genes specific to hemocytes. These situations, however, do not reduce the significance of the TCs listed in the tables. As described above, these TCs that represent abundantly and preferentially expressed transcripts should reflect characteristic features associated with gene expression in *Ciona* hemocytes.

Acknowledgements: We would like to express our thanks to K. Hirayama for preparing the *Ciona* samples and M. Kuji for preparing the manuscript, respectively. This work was supported in part by research grants from the Ministry of Education, Science, Sports, Culture, and Technology, Japan. M.S. is a member of the 21st century COE program, "Center for Innovative Therapeutic Development Towards the Conquest of Signal Transduction Diseases" which is headed by K. Sugamura at Tohoku University.

References

1. Laird, D. J., De Tomaso, A. W., Cooper, M. D. et al. 2000, 50 million years of chordate evolution: seeking the origins of adaptive immunity, *Proc. Natl. Acad. Sci. USA*, **97**, 6924–6926.
2. Azumi, K., De Santis, R., De Tomaso, A. et al. 2003, Genomic analysis of immunity in a urochordate and the emergence of the vertebrate immune system: "waiting for Godot," *Immunogenetics*, **55**, 570–581.
3. Dehal, P., Satou, Y., Campbell, R. K. et al. 2002, The draft genome of *Ciona intestinalis*: insights into chordate and vertebrate origins, *Science*, **298**, 2157–2167.
4. Satoh, N., Satou, Y., Davidson, B. et al. 2003, *Ciona intestinalis*: an emerging model for whole-genome analyses, *Trends in Genetcs*, **19**, 376–381.
5. Wright, R. K. 1974, Protochordate immunity: primary immune response of the tunicate *Ciona intestinalis* to vertebrate erthrocytes, *J. Inverteb. Pathol.*, **24**, 29–36.
6. Ohtake, S., Abe, T., Shishikura, F. et al. 1994, The phagocytes in hemolymph of *Halocynthia roretzi* and their phagocytic activity, *Zool. Sci.*, **11**, 681–691.
7. Azumi, K., Ishimoto, R., Fujita, T. et al. 2000, Opsonin-independent and -dependent phagocytosis in the ascidian *Halocynthia roretzi*: galactose-specific lectin and complement C3 function as target-dependent opsonins, *Zool. Sci.*, **17**, 625–632.
8. Azumi, K., Yokosawa, H., and Ishii, S. 1990, Halocyamines: novel antimicrobial tetrapeptide-like substances isolated from the hemocytes of the solitary ascidian *Halocynthia roretzi*, *Biochemistry*, **29**, 159–165.
9. Lee, I. H., Zhao, C., Cho, Y. et al. 1997, Clavanins, alpha-helical antimicrobial peptides from tunicate hemocytes, *FEBS Lett.*, **400**, 158–162.
10. Lee, I. H., Cho, Y., and Lehrer, R. I. 1997, Styelins, broad-spectrum antimicrobial peptides from the solitary tunicate, *Styela clava*, *Comp. Biochem. Physiol. B*, **118**, 515–521.
11. Lee, I. H., Lee, Y. S., Kim, C. H. et al. 2001, Dicynthaurin: an antimicrobial peptide from hemocytes of the solitary tunicate, *Halocynthia aurantium*, *Biochim. Biophys. Acta*, **1527**, 141–148.
12. Shida, K., Terajima, D., Uchino, R. et al. 2003, Hemocytes of *Ciona intestinalis* express multiple genes involved in innate immune host defense, *Biochem. Biophys. Res. Commun.*, **302**, 207–218.
13. Terajima, D., Yamada, S., Uchino, R. et al. 2003, Identification and sequence of seventy-nine new transcripts expressed in hemocytes of *Ciona intestinalis*, three of which are possibly involved in characteristic cell-cell communication, *DNA Res.*, **10**, 203–212.
14. Satou, Y., Takatori, N., Yamada, L. et al. 2001, Gene expression profiles in *Ciona intestinalis* tailbud embryos, *Development*, **128**, 2893–2904.
15. Satou, Y., Takatori, N., Fujiwara, S. et al. 2002, *Ciona intestinalis* cDNA projects: expressed sequence tag analyses and gene expression profiles during embryogenesis, *Gene*, **287**, 83–96.
16. Satou, Y., Yamada, L., Mochizuki, Y. et al. 2002, A cDNA resource from the basal chordate *Ciona intestinalis*, *Genesis*, **33**, 153–154.
17. Inaba, K., Padma, P., Satouh, Y. et al. 2002, EST analysis of gene expression in testis of the ascidian *Ciona intestinalis*, *Mol. Reprod. Dev.*, **62**, 431–445.
18. Nishikata, T., Yamada, L., Mochizuki, Y. et al. 2001, Profiles of maternally expressed genes in fertilized eggs of *Ciona intestinalis*, *Dev. Biol.*, **238**, 315–331.
19. Fujiwara, S., Maeda, Y., Shin-I, T. et al. 2002, Gene expression profiles in Ciona intestinalis cleavage-stage embryos, *Mech. Dev.*, **112**, 115–127.
20. Kusakabe, T., Yoshida, R., Kawakami, I. et al. 2002, Gene expression profiles in tadpole larvae of *Ciona intestinalis*, *Dev. Biol.*, **242**, 188–203.
21. Ogasawara, M., Sasaki, A., Metoki, H. et al. 2002, Gene expression profiles in young adult *Ciona intestinalis*, *Dev.*

Genes Evol., **212**, 173–185.
22. Miyazawa, S., Azumi, K., and Nonaka, M. 2001, Cloning and characterization of integrin subunits from the solitary ascidian, *Halocynthia roretzi*, *J. Immunol.*, **166**, 1710–1715.
23. Azumi, K., Satoh, N., and Yokosawa, H. 1993, Functional and structural characterization of hemocytes of the solitary ascidian, *Halocynthia roretzi*, *J. Exp. Zool.*, **265**, 309–316.
24. Altschul, S. F., Madden, T. L., Schaffer, A. A. et al. 1997,Gapped BLAST and PSI-BLAST: a new generation of protein database search programs, *Nucl. Acids Res.*, **25**, 3389–3402.
25. Schultz, J., Milpetz, F., Bork, P. et al. 1998, SMART, a simple modular architecture research tool: identification of signaling domains, *Proc. Natl. Acad. Sci. USA*, **95**, 5857–5864.
26. Ogasawara, M., Minokawa, T., Sasakura, Y. et al. 2001, A large-scale whole-mount *in situ* hybridization system: rapid one-tube preparation of DIG-labeled RNA probes and high throughput hybridization using 96-well silent screen plates, *Zool. Sci.*, **18**, 187–193.

First-principles study of the electronic structures of icosahedral Ti_N (N=13,19,43,55) clusters

Shan-Ying Wang[a)]
Institute for Materials Research, Tohoku University, Aoba-ku, Sendai 980-8577, Japan and Department of Physics, Tsinghua University, Beijing 100084, China

Jing-Zhi Yu and Hiroshi Mizuseki
Institute for Materials Research, Tohoku University, Aoba-ku, Sendai 980-8577, Japan

Jia-An Yan
Department of Physics, Tsinghua University, Beijing 100084, China

Yoshiyuki Kawazoe
Institute for Materials Research, Tohoku University, Aoba-ku, Sendai 980-8577, Japan

Chong-Yu Wang
Department of Physics, Tsinghua University, Beijing 100084, China and Center Iron and Steel Research Institute, Beijing 100081, China

(Received 29 December 2003; accepted 20 February 2004)

We have studied the electronic structures of icosahedral Ti_N clusters (N=13, 19, 43, and 55) by using a real-space first-principles cluster method with generalized gradient approximation for exchange-correlation potential. The hexagonal close-packed and fcc close-packed clusters have been studied additionally for comparisons. It is found that the icosahedral structures are the most stable ones except for Ti_{43}, where fcc close-packed structure is favorable in energy. We present and discuss the variation of bond length, the features of the highest occupied molecular orbitals and the lowest unoccupied molecular orbital, the evolution of density of states, and the magnetic moment in detail. The results are in good agreement with the predictions from the collision-induced dissociation and size-selected anion photoelectron spectroscopy experiments. © *2004 American Institute of Physics.* [DOI: 10.1063/1.1701769]

I. INTRODUCTION

Transition-metal clusters have received much scientific and technological interest and been widely studied in the recent two decades.[1] They show the distinction of complexity in both geometrical structure and magnetism. The localized and unfilled d shells usually result in spin multiplets and low-lying energy states that bring many useful physical and chemical properties for transition-metal clusters, making them highly promising in nanotechnological applications.

The evolution of electronic structure from atoms to the bulk is an important question, involving the evolutions of bond length, density of states (DOS), magnetic moment, and the energy gap between the highest occupied molecular orbital (HOMO) and the lowest unoccupied molecular orbital (LUMO). The clusters of medium size consisting of tens to several tens atoms are particularly important in the research. To our knowledge, clusters composed of the later part of $3d$ elements such as Mn, Fe, Co, and Ni have been widely studied.[2–9] For medium-size V, Ti, and Cr clusters, the geometrical structure, electronic structure, and magnetism are still unknown even though they are believed to be simple and expected to show some bulk features. Size-selected anion photoelectron spectroscopy (PES) is powerful experimental technique for exploring the electronic structure of clusters, with which Wang's group has obtained many valuable and meaningful results on transition-metal clusters.[10–15] Their experiments on Ti clusters[10,11] have shown that the pronounced narrowing of PES features occurs for Ti_{13}^- and Ti_{55}^-, and the $3d$ band emerges at the eight-atom cluster, beyond which the d band broadens and evolves toward that of the bulk. These and another collision-induced dissociation experiment[16] suggest that Ti_{13}, Ti_{19}, and Ti_{55} clusters prefer an icosahedral structure. More recently, Castro *et al.* also reported their first-principles study of the ultrafine Ti_N and Ti_N^{-1} (N=3–8,13) clusters,[17] where the theoretical results are in good agreement with their experimental results. In the previous study of icosahedral Ti_{13} clusters,[18] we found that the bonding feature in the cluster is close to that in the hexagonal bulk Ti obtained by energy band calculations.[19] However, the characteristic bond lengths (2.57 and 2.70 Å) are much shorter than that (2.95 Å) of bulk Ti.

Actually it is still difficult to detect only by experimental approaches the exact geometrical structure of clusters. Nevertheless, associating with the experimental measurements, scientists can predict effectively and accurately some unknown structures by employing the first-principles method based on density functional theory (DFT).[20,21] In the present work, we study the electronic structure of icosahedral (ico) Ti_N clusters (N=13, 19, 43, and 55) by using a real-space first-principles cluster method named density functional for molecules (DMol).[22,23] Bulk Ti shows the hexagonal close-

a)Electronic mail: sywang@imr.edu

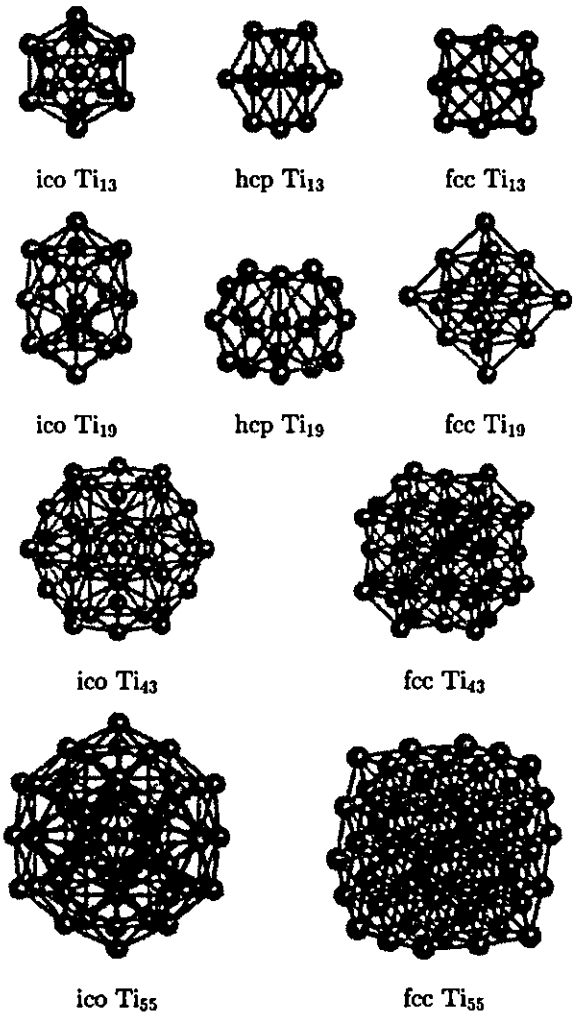

FIG. 1. The ico, hcp, and fcc structures of Ti clusters.

packed (hcp) instead of the fcc close-packed (fcc) phase at low temperature. For comparison, the studies of the hcp structures of Ti_{13} and Ti_{19} and the fcc structures of Ti_{13}, Ti_{19}, Ti_{43}, and Ti_{55} are included. We present and discuss the binding energy, bond length, HOMO and LUMO states, DOS, and magnetism in detail.

II. METHOD AND COMPUTATIONAL DETAILS

DMol is a widely used real-space first-principles cluster method based on DFT and has been applied to many problems on molecular clusters, chemisorption, surface reconstruction, and the ground state of highly correlated transition-metal clusters. It performs accurate and efficient self-consistent calculations and structural optimization by using, respectively, a fast-convergent three-dimensional numerical integration scheme and several effective local-minimum searching techniques. The equilibrium structure and total energy can be obtained by relaxing atoms until the forces are deemed to be zero.

In first-principles calculations, one must minimize as far as possible the effects of the basis and the exchange-correlation functional on the results. The inner orbitals such as $3s$ and $3p$ sometimes are important for the ground-state properties of transition metals. This is particularly true for ultrafine Ti clusters.[24] We choose a double-numerical basis with polarized functions and only froze the $1s2s2p$ orbitals in the calculations. The general gradient approximation (GGA) is used by combining the correlation functional of Perdew[25] with exchange functional of Becke.[26] All calculations are spin unrestricted. The parameters used here were tested by Ti_2 dimes.[18] For accurate calculations, we choose an octuple scheme for the multipolar fitting procedure (the maximum angular momentum of the fitting function is set to be 3) on the charge density and Coulomb potential and a fine grid scheme for numerical integration (about 1500 integration points per atom). In the optimizations, the energy gradient and atomic displacement are converged to 0.03 eV $Å^{-1}$ and 5×10^{-4} Å, respectively. The charge density in the self-consistent iterations is converged to 1×10^{-5}, which allows a total energy convergence of 1×10^{-4} eV. The binding energy (BE) is defined as

$$\mathrm{BE}=E_a-E_t,$$

where E_a is the sum of the total energies of all single atoms and E_t is the total energy of the cluster.

Figure 1 shows the geometrical structures of the clusters. All the hcp and fcc structures are generated originally from the bulk state according to the neighboring relationship. The ico Ti_{43} cluster is generated by adding 30 atoms on top of edge positions of the ico Ti_{13} cluster and ico Ti_{55} cluster by adding additional 12 atoms on top of vertex positions. In structural optimizations, all atoms are relaxed freely under a symmetrical restriction—i.e., holding I_h, O_h, and D_{3h} symmetries for Ti_{13} and Ti_{19} clusters and D_{5d} and O_h symmetries for Ti_{43} and Ti_{55} clusters. For a technical reason from the DMol executive code, we have to use subgroup D_{5d} instead of I_h to reduce the Hamiltonian matrix in the calculation for ico Ti_{43} and Ti_{55} clusters. This can be taken as a very weak Jahn–Teller effect and has little effect on the discussion, since the energy levels near the Fermi level show much slight splitting (not beyond 0.006 eV, nearly degenerate states) and those bonds that are equivalent at I_h symmetry show little difference in length (usually not beyond 1% except for only two bonds change by about 3% in Ti_{43}). For an easy discussion, we will use the averaged quantities (bond length and atomic magnetic moment) for those atoms that are equivalent at I_h symmetry.

TABLE I. Calculated binding energies in eV for the ico, hcp, and fcc structures. The binding energy per atom is included in the parentheses.

	Ti_{13}	Ti_{19}	Ti_{43}	Ti_{55}
ico	54.20(4.17)	82.81(4.36)	188.52(4.38)	259.43(4.72)
hcp	51.48(3.96)	80.83(4.25)		
fcc	50.77(3.91)	77.17(4.06)	194.34(4.52)	255.88(4.65)

III. RESULT AND DISCUSSION

All data on ico Ti_{13} cluster listed in Tables I–IV are quoted from our previous work.[18]

TABLE II. Calculated bond lengths in Å and the corresponding bond numbers in the ico, hcp, and fcc structures. The averaged bond length and total number of effective bonds of cluster are also given. l_{ij} denotes the length of the bond formed by atoms in the ith and jth shells with respect to the center of cluster (atom at the center is indexed by the zeroth shell except for icosahedral Ti_{19} cluster, where the two inner atoms are indexed by the zeroth shell). The bonds are counted within an 2.95 Å cutoff in length (a characteristic bond length of bulk Ti). For Ti_{43} and Ti_{55}, l_{02}, l_{03}, and l_{04} are given additionally for showing the radii of the shells.

Ti_{13}			Ti_{19}			Ti_{43}			Ti_{55}		
ico	l_{01}	2.567,12	ico	l_{00}	2.324,1	ico	l_{01}	2.754,12	ico	l_{01}	2.720,12
	l_{11}	2.699,30		l_{01}	2.464,2		l_{11}	2.896,30		l_{11}	2.867,30
					2.545,10		l_{12}	2.614,60		l_{12}	2.722,60
hcp	l_{01}	2.585,6			2.811,10		l_{22}	2.793,60		l_{13}	2.436,12
		2.680,6		l_{11}	2.684,10		l_{02}	4.519,30		l_{22}	2.864,60
	l_{11}	2.518,3			2.707,10					l_{23}	2.723,60
		2.613,6			2.714,20	fcc	l_{01}	2.819,12		l_{02}	4.634,30
		2.651,3					l_{11}	2.819,24		l_{03}	5.159,12
		2.656,12	hcp	l_{01}	2.799,6		l_{12}	2.698,24			
				l_{11}	2.284,3		l_{13}	2.659,48	fcc	l_{01}	2.760,12
fcc	l_{01}	2.648,12			2.725,12		l_{23}	2.730,24		l_{11}	2.760,24
	l_{11}	2.648,24			2.943,6		l_{33}	2.673,24		l_{12}	2.750,24
				l_{12}	2.470,12		l_{02}	3.811,6		l_{13}	2.765,48
					2.527,12		l_{03}	4.696,24		l_{14}	2.622,12
										l_{23}	2.793,24
			fcc	l_{01}	2.754,12					l_{33}	2.704,24
				l_{11}	2.754,24					l_{34}	2.694,48
				l_{12}	2.656,24					l_{02}	3.889,6
										l_{03}	4.786,24
										l_{04}	5.382,12
ico	2.661,42			2.683,63			2.743,162			2.762,234	
hcp	2.629,36			2.627,51							
fcc	2.648,36			2.715,60			2.715,156			2.735,216	

A. Binding energy

The calculated BEs are listed in Table I. For the Ti_{13} cluster, the ico structure is the lowest-energy state and the BE is 54.20 eV, larger than those of hcp and fcc structures by about 2.72 and 3.43 eV, respectively. Similarly, the ico Ti_{19} shows the highest BE 82.81 eV, about 1.98 and 5.64 eV larger than those of hcp and fcc structures, respectively. For Ti_{43}, however, the fcc structure becomes the lower-energy state and the BE is 194.34 eV, about 5.82 eV larger than that of ico structure. For Ti_{55}, the ico structure has again the higher BE 259.43 eV, about 4.55 eV larger than that of fcc structure. These results suggest that the ico Ti_{13}, Ti_{19}, and Ti_{55} and the fcc Ti_{43} clusters are favorable in energy, which are in agreement with the predictions from the size-selected anion PES and the collision-induced dissociation experiments.[10,11,16] In fact, no evidence has been found in the PES experiments that the Ti_{43} cluster will prefer an ico structure. On the contrary, the PES experiments support a tentative conclusion that the medium-size Ti clusters may possess bcc-type structure since the medium-size anion Ti clusters show similar two-band features in PES spectra as anion V clusters. The cluster packing for the medium-size Ti cluster is very complicated and needs further investigation from both experiment and theoretical calculations. Table I also gives the calculated BE per atom. For those structures favorable in energy, the BE per atom increases smoothly from Ti_{13} to Ti_{55} (4.17, 4.36, 4.52, and 4.72 eV) and can be expected to approach the cohesive energy of bulk Ti (4.85 eV per atom) for larger Ti clusters.

B. Bond length

Table II gives the results of the calculated bond lengths (BLs) and the bond numbers in the ico, hcp, and fcc structures. The bonds are counted by a reasonable cutoff 2.95 Å (a characteristic bond length of bulk Ti), within which the interaction between the two atoms are believed to be effective. We call these bonds as effective bonds (EBs). We classify all atoms by shells according to their neighboring relationship with respect to the center of the cluster (the atom at the center is indexed by the zeroth shell). Note that for ico Ti_{19} (it is indeed a bi-icosahedral structures), since there is no atom at its center, we simply group the 19 atoms into two shells and index the two inner atoms (refer to Fig. 1) by the zeroth shell. All bonds are denoted by the shell index in Table II.

We first discuss the BL variations in the *ico structure*. For Ti_{19}, the two inner atoms have the shortest BL (l_{00} = 2.324 Å), which implies a strong interaction between them. Comparing with Ti_{13}, the two BLs l_{01} in the main symmetry axis decrease to a rather short value 2.464 Å. Most of the BLs (l_{11}) in the first shell increase. The results indicate that the bi-icosahedral structure of Ti_{19} shrinks along its main symmetry axis, but expands transversely compared with Ti_{13}. For Ti_{43}, we can see an interesting phenomenon that the second shell makes the first shell expand. Compared with Ti_{13} and Ti_{19}, the l_{01} and l_{11} keep on increasing and those EBs within the first shell are weakened. The l_{22} takes a relatively large value 2.793 Å while the l_{12} shows a relatively short value 2.614 Å, indicating that the EBs (l_{12}) be-

TABLE III. Calculated HOMO and LUMO states in the ico, hcp, and fcc structures. The symbols "+" and "−" denote the spin-up and spin-down states, respectively. E denotes the energy in eV and n denotes the electron occupation number.

	ico			hcp			fcc		
	State	E	n	State	E	n	State	E	n
Ti_{13}	T1U(−)	−3.886	2	$E'(-)$	−3.588	1	T2U(±)	−3.369	6
	HG(−)	−3.741	0	$A2'(-)$	−3.454	0	T1U(±)	−3.213	0
Ti_{19}	$E1''(+)$	−3.961	2	$E''(\pm)^-$	−3.807	2	T2U(+)	−3.793	3
	$E1''(-)$	−3.846	0	$A2'(\pm)$	−3.736	0	$A2U(+)$	−3.772	0
Ti_{43}	$A1G(-)$	−3.596	1				T2G(−)	−3.586	2
	$A2U(-)$	−3.563	0				$A1G(+)$	−3.578	0
Ti_{55}	$E2G(\pm)$	−4.279	4				T1G(+)	−3.899	3
	$A1U(\pm)$	−4.114	0				T1U(+)	−3.887	0

tween the first and second shells become more important for the binding property of Ti_{43}. For Ti_{55}, due to the presence of the third shell, the first shell is contracted and the second shell expands somewhat compared to those of Ti_{43}. Consequently, the l_{11} decreases while the l_{12} and l_{22} increases. The BLs between the neighboring different shells (l_{01}, l_{12}, and l_{23}) in Ti_{55} show little difference (not beyond 0.003 Å) and reach basically to an equilibrium state. Surprisingly, the first shell still has 12 strong EBs (l_{13}=2.436 Å) with the third shell in Ti_{55}. For all ico structures, it can be found that the EBs between the different shells (l_{01}, l_{12}, l_{13}, and l_{23}) are shorter than those in the same shell (l_{11} and l_{22}) except for the 11 EBs (l_{00}=2.324 Å, l_{01}=2.811 Å) in the bi-icosahedral structure of Ti_{19}. It seems that the interactions between the different shells are more important than those in the same shells for the binding property of medium-size ico Ti clusters.

Now we discuss the case in the *hcp and fcc structures*. For hcp Ti_{13}, the l_{01} increases and l_{11} reduces to some extent compared with those in the ico structure. For hcp Ti_{19}, all EBs within the first shell expand remarkably compared with those in Ti_{13} except for the three EBs in the hexagonal ring, which, however, decrease greatly (l_{11}=2.284 Å) and become the strongest. Note the other three EBs in the hexagonal ring are destroyed: the 24 EBs (l_{11}) in Ti_{13} decrease to the 21 EBs in Ti_{19}. The EBs between the first and second shells in hcp Ti_{19} are much stronger since they show relatively short values in length (l_{12}=2.470,2.527 Å). For all fcc structures, it is interesting that the BLs between the center atom and the atoms in the first shell are equal to those between the atoms in the first shell ($l_{01}=l_{11}$). The variation features of EB from fcc Ti_{13} to Ti_{55} are similar to the case of ico structures. From fcc Ti_{13} to Ti_{43}, the BLs l_{01}, l_{11}, and l_{12} increase continuously, indicating the expanding of the first and second shells. Compared with fcc Ti_{43}, the first shell in fcc Ti_{55} shrinks somewhat while the second shell expands largely.

It can be seen that the ico structure has more EBs than the hcp and fcc structures. However, the averaged BL of ico structure is not the shortest. It seems that the binding energy is not directly or explicitly related to these quantities.

C. HOMO and LUMO states

Table III presents data on the HOMO and LUMO states. For ico clusters, the HOMO–LUMO gaps are comparatively large, beyond 0.14 eV, with the exception of a much small value ~0.03 eV for Ti_{43}. All the ico clusters are spin polarized except for Ti_{55}, which has fully paired electrons and becomes a closed-shell system. The ico Ti_{19} is a semifilled open-shell system while Ti_{13} and Ti_{43} have additional unpaired electrons in molecular orbitals besides the HOMO. For hcp clusters, Ti_{13} is an open-shell system with a comparatively large HOMO–LUMO gap ~0.13 eV and Ti_{19} is a closed-shell system with a small one ~0.07 eV. For fcc clusters, Ti_{13} is a closed-shell system, and Ti_{43} and Ti_{55} show near-zero HOMO–LUMO gaps.

D. Density of states and magnetism

The size-selected anion PES experiments[10,11] have shown that the $3d$ band emerges at the eight-atom Ti cluster, and broadens and evolves toward the bulk characteristics with the increase of cluster size. In order to well understand the phenomena observed in the experiment, we present the total DOS and spin-dependent total DOS of ico Ti_{13}, Ti_{19}, Ti_{55}, and fcc Ti_{43} clusters in Figs. 2 and 3, respectively. The total DOS is calculated by broadening the energy levels ε_i of molecular orbitals by using a line-shape function Lorentzian with width δ=0.1 eV as follows:

$$\mathrm{DOS}(E)=\sum_i \frac{\delta/\pi}{(E-\varepsilon_i)^2+\delta^2}.$$

Two significant resonant peaks A and B as shown in Fig. 2 can be identified from the onset of DOS of valent states, which are both $s,p-d$ hybridizations states. With the increasing of cluster size, the two peaks decompose somewhat and become more structurized, and the site difference between their spectral centers decreases from about 2.5 to 1.5 eV by a rough evaluation. These results are basically in agreement with the PES experiment, where a two-band structure with a site difference of about 1.5 eV was observed for medium-size Ti clusters. For PES, it is not surprising that there are differences between the experiment and first-principles calculation, since the DFT used in most of the first-principles methods is still a ground-state theory. However, PES is involved in very complicated electronic exciting process.

There are several features displaying how the DOS evolves from Ti_{13} to Ti_{55}. First, a little peak of $4s$ states

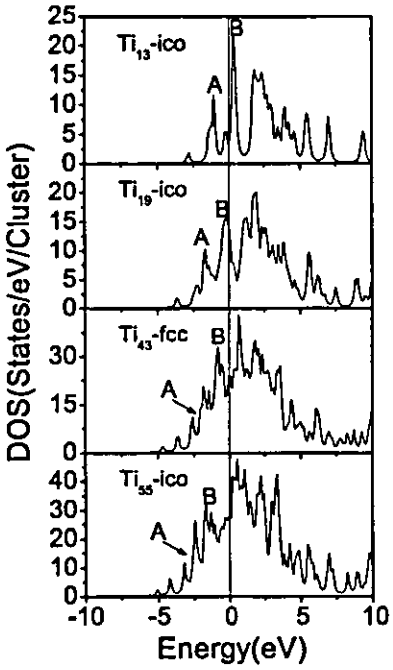

FIG. 2. The total DOS of the ico Ti_{13}, Ti_{19}, Ti_{55}, and fcc Ti_{43} clusters. The Fermi level is shifted to zero.

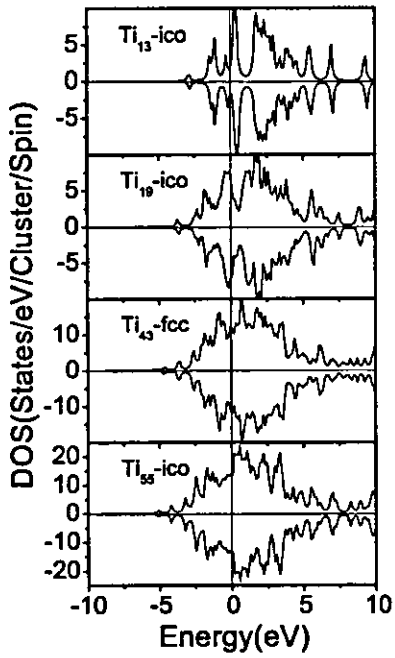

FIG. 3. The spin-dependent total DOS of the ico Ti_{13}, Ti_{19}, Ti_{55}, and fcc Ti_{43} clusters. The spin-up and spin-down states are displayed in the up panel (plus value) and down panel (minus value), respectively. The Fermi level is shifted to zero.

appearing at the initial position of DOS curve shifts to the lower-energy positions and the peak value reduces successively from Ti_{13} to Ti_{55}. Next, there is a remarkably deep valley around 1.2 eV in Ti_{13}, which dwindles largely in size in Ti_{19} and disappears in Ti_{43} and Ti_{55}. Then, closely associating with the above two features, the DOS spreads out to a relatively wide energy range from Ti_{13} to Ti_{55}. Finally, we can notice that the appearance of the total DOS of Ti_{55} is very close to that of bulk Ti.[19,27] Particularly, the DOS that locate within the energy range crossing the Fermi level from about -2.2 to 2.2 eV show similar variation characteristics as the bulk Ti: a large extended peak followed by an ascent crossing the Fermi level, and then comes another large extended peak. One can expect that the features of the DOS of bulk Ti will be present more completely in larger clusters than Ti_{55}. It may be reasonable to take approximately the above features as the DOS evolution from cluster to bulk.

On the other hand, unlike other transition-metal clusters, these medium-size Ti clusters show complex $s,p-d$ hybridization states rather than distinct $3d$ localized characteristics. We can see that the hybridization states span a relatively wide energy range. These features actually are closely related to the electronic configuration of the Ti atom. Due to the fewer electrons occupying $3d$ orbitals, the Ti atom has relatively expanded $3d$ states in space compared to the latter part of $3d$ elements like Fe, Co, and Ni. These $3d$ states are easily delocalized by $s,p-d$ hybridizations, which appears to result in a weak magnetism for Ti clusters. It can be seen from Fig. 3 that the ico Ti_{13} and Ti_{19} and the fcc Ti_{43} clusters show just slight exchange splittings and possess total magnetic moments of $(6.0,2.0,4.0)\mu_B$, respectively (see Table IV). The ico Ti_{55} is nonmagnetic and there is no exchange splitting in total DOS. For Ti_{13}, the state of $0.0\mu_B$ is about 0.61 eV higher than the ground state of $6.0\mu_B$. Castro *et al.* have reported a ground state of $0.0\mu_B$ (closed shell state) with the state of $2.0\mu_B \sim 0.03$ eV higher.[17] This discrepancy mainly comes from the differences for treating spin and symmetry. We obtained the states of $6.0\mu_B$ ($0.0\mu_B$) by using a pure spin-polarized (spin-unpolarized) mode instead of a constraint on the total-spin state of the cluster (singlet and triplet) as used by Castro *et al.* Nevertheless, both ways can yield a reasonable description of the magnetism of transition-metal clusters and further experiments on the magnetism of Ti clusters is necessary for examination. On the other hand, we used an I_h symmetry constraint in the structural optimi-

TABLE IV. Calculated atomic magnetic moments in μ_B in ico Ti_{13}, Ti_{19}, and Ti_{55} and fcc Ti_{43} clusters. The total magnetic moment of cluster is also given either. The numbers 0, 1, 2, and 3 index the atomic shells with respect to the center of cluster (atom at the center is indexed by the zeroth shell except for icosahedral Ti_{19} cluster, where the two inner atoms are indexed by the zeroth shell).

	0	1	2	3	Total
Ti_{13} (ico)	0.202	0.483			6.000
Ti_{19} (ico)	−0.054	0.124			2.000
Ti_{43} (fcc)	0.169	−0.010	0.209	0.112	4.000
Ti_{55} (ico)	0.000	0.000	0.000	0.000	0.000

zation and Castro *et al.* did without symmetry—i.e., full optimization. It should be pointed out that as a result of spin polarization, even for the deeper occupied molecular orbitals, its spin-up and spin-down states can be nondegenerate. The total magnetic moment of clusters is determined by the difference between the electron numbers in the spin-up and spin-down molecular orbitals. Thus we can see from Tables III and IV that Ti_{13} has a total magnetic moment of $6.0\mu_B$; i.e., there are totally six unpaired spin-up electrons, while there are two spin-down electrons in its HOMO. The center atom of ico Ti_{13} forms spin ferromagnetic states with its 12 neighboring atoms, whereas the inner two atoms of ico Ti_{19} form spin antiferromagnetic states with the outside atoms. For fcc Ti_{43}, the atomic magnetic moments in the first shell are antiparallel with all others in the cluster. The atomic magnetic moments in ico Ti_{55}, however, are completely quenched. Usually, the enhanced local magnetic moments are expected to appear in the low-dimensional systems of transition-metal-like clusters, surfaces, and interfaces, where the lower symmetry and coordination number are two favorable factors for magnetism. Such a property, however, seems not extend to Ti since these medium-size clusters just show very weak magnetism compared to nonmagnetic bulk Ti.

IV. CONCLUSION

The first-principles DMol method based on DFT with the GGA is employed for studying the electronic structures of the icosahedral, hexagonal close-packed, and fcc close-packed Ti_N clusters ($N=13$, 19, 43, and 55). For all these medium-size clusters, the icosahedral structures are found to be favorable in energy except for Ti_{43}, where the fcc close-packed structure is the lower-energy state. With the increase of cluster size, the atomic shells show complex expanding or shrinking behaviors. The bonding between the different atomic shells is more important for the binding property of icosahedral structure. The icosahedral structure has more effective bonds and a longer averaged bond length than the hexagonal close-packed and fcc close-packed structures. The icosahedral Ti_{13} and fcc close-packed Ti_{43} are open-shell systems with additional unpaired electrons in molecular orbitals besides the HOMO. The icosahedral Ti_{19} and Ti_{55} are, respectively, a semifilled open-shell system and closed-shell system, and the latter has the largest HOMO–LUMO gap ~0.17 eV. The total DOS, particularly those states near the Fermi level of icosahedral Ti_{55}, are very close to that of bulk Ti. The variation of the DOS from Ti_{13} to Ti_{55} indicates approximately the DOS evolution from cluster to bulk. All clusters show strong $s,p-d$ hybridization states, which result in a very weak magnetism of icosahedral Ti_{13}, Ti_{19}, and fcc close-packed Ti_{43} and quenched atomic magnetic moments in icosahedral Ti_{55}. The results are in agreement with the predictions from the collision-induced dissociation and size-selected anion photoelectron spectroscopy experiments.

ACKNOWLEDGMENTS

We thank the crew of the Center for Computational Materials Science (CCMS) of the Institute for Materials Research (IMR), Tohoku University, Japan, for their support of computing facilities. This work was partially supported by "973" Project from the Ministry of Science and Technology of the People's Republic of China (Grant No. G2000067102).

[1] J. A. Alonso, Chem. Rev. **100**, 637 (2000).
[2] Z. Q. Li and B. L. Gu, Phys. Rev. B **47**, 13611 (1993).
[3] F. A. Reuse and S. N. Khanna, Chem. Phys. Lett. **234**, 77 (1995).
[4] F. A. Reuse, S. N. Khanna, and S. Bernel, Phys. Rev. B **52**, R11650 (1995).
[5] P. Ballone and R. O. Jones, Chem. Phys. Lett. **233**, 632 (1995).
[6] N. N. Lathiotakis, A. N. Andriotis, M. Menon, and J. Connolly, J. Chem. Phys. **104**, 992 (1996).
[7] M. Castro, Int. J. Quantum Chem. **64**, 223 (1997).
[8] Tina M. Briere, Marcel H. F. Sluiter, V. Kumar, and Y. Kawazoe, Mater. Trans., JIM **43**, 424 (2002).
[9] Tina M. Briere, Marcel H. F. Sluiter, V. Kumar, and Y. Kawazoe, Phys. Rev. B **66**, 064412 (2002).
[10] H. B. Wu, S. R. Desai, and L. S. Wang, Phys. Rev. Lett. **76**, 212 (1996).
[11] S. R. Liu, H. J. Zhai, M. Castro, and L. S. Wang, J. Chem. Phys. **118**, 2108 (2003).
[12] S. R. Liu, H. J. Zhai, and L. S. Wang, Phys. Rev. B **64**, 153402 (2001).
[13] S. R. Liu, H. J. Zhai, and L. S. Wang, Phys. Rev. B **65**, 113401 (2002).
[14] S. R. Liu, H. J. Zhai, and L. S. Wang, J. Chem. Phys. **117**, 9758 (2002).
[15] L. S. Wang, X. Li, and H. F. Zhang, Chem. Phys. **262**, 53 (2000).
[16] L. Lian, C.-X. Su, and P. B. Armentrout, J. Chem. Phys. **97**, 4084 (1992).
[17] M. Castro, S. R. Liu, H. J. Zhai, and L. S. Wang, J. Chem. Phys. **118**, 2116 (2003).
[18] S. Y. Wang, W. H. Duan, D. L. Zhao, and C. Y. Wang, Phys. Rev. B **65**, 165424 (2002).
[19] O. Jepson, Phys. Rev. B **12**, 2988 (1975).
[20] P. C. Hohenberg and W. Kohn, Phys. Rev. **136**, B864 (1964).
[21] W. Kohn and L. J. Sham, Phys. Rev. **140**, A1133 (1965).
[22] B. Delley, J. Chem. Phys. **92**, 508 (1990).
[23] B. Delley, J. Chem. Phys. **94**, 7245 (1991).
[24] S. H. Wei, Z. Zeng, J. Q. You, X. H. Yan, and X. G. Gong, J. Chem. Phys. **113**, 11127 (2000).
[25] J. P. Perdew and Y. Wang, Phys. Rev. B **45**, 13244 (1992).
[26] A. D. Becke, Phys. Rev. A **38**, 3098 (1988).
[27] V. L. Moruzzi, J. F. Janak, and A. R. Williams, *Calculated Electronic Properties of Metals* (Pergamon, New York, 1978).

Energetics and local spin magnetic moment of single 3,4*d* impurities encapsulated in an icosahedral Au_{12} cage

Shan-Ying Wang,[1,2,*] Jing-Zhi Yu,[1] Hiroshi Mizuseki,[1] Qiang Sun,[3] Chong-Yu Wang,[2] and Yoshiyuki Kawazoe[1]
[1]*Institute for Materials Research, Tohoku University, Aoba-ku, Sendai 980-8577, Japan*
[2]*Department of Physics, Tsinghua University, Beijing 100084, People's Republic of China*
[3]*Physics Department, Virginia Commonwealth University, Richmond, Virginia 23284-2000, USA*
(Received 7 April 2004; revised manuscript received 1 June 2004; published 21 October 2004)

The energetics and local spin magnetic moment of a single 3,4*d* impurity (Sc-Ni, Y-Pd) encapsulated in an icosahedral Au_{12} cage have been studied theoretically by using a real-space first-principles cluster method with generalized gradient approximation for exchange-correlation functional. The relativistic effect is considered by scalar relativistic pseudopotentials. All doped clusters show unexpected large relative binding energies compared with icosahedral Au_{13} cluster. The smallest and the largest values appear at Pd and Zr, 2.186 and 7.791 eV per cluster, respectively, indicating doping could stabilize the icosahedral Au_{12} cage and promote the formation of a new binary alloy cluster. Comparatively large magnetic moments are observed for 3*d* elements Cr, Mn, Fe, Co, and Ni (2.265, 3.512, 3.064, 1.947, and 0.943 μ_B), and 4*d* elements Tc, Ru, and Rh (0.758, 1.137, and 0.893 μ_B). The density of states and the relativistic effects on electronic structure are discussed.

DOI: 10.1103/PhysRevB.70.165413 PACS number(s): 31.15.Ar, 36.40.Cg, 36.40.Qv

I. INTRODUCTION

Single transition metal element isolated in an *sp* metal host is a classical ideal system for studying how the *d* electron interact with nearly free electron gas to form a local magnetic moment (LMM).[1–4] The recent advanced synthesis techniques are making scientists able to explore such a problem in many different types of system. For example, it has been shown experimentally that transition metal element can also display unusual large LMM when absorbed on or embedded into an *sp* metal surface.[5,6] The LMM of transition metal element is rather sensitive to the environment, and adjusted dramatically by the shape and size of the environment formed by the host atoms. From this point of view, one can design many different types of system for studying the local magnetism problem. For example, a single 3,4*d* impurity encapsulated in an *sp* metal cage may be an interesting system. The idea of doping an impurity into a cluster cage initially appeared in the work[7,8] of Callaway and Dunlap, and then extended explicitly by Gong, Kumar, Sun, and Kawazoe as studying the stability and local magnetic properties of 3,4*d* impurities encapsulated in icosahedral Al_{12}, Cu_{12}, and Ag_{12} cages.[9–11] These theoretical works predicted that some 3,4*d* impurities could show relatively large local spin magnetic moments (LSMM's) when encapsulated in an *sp* metal cage.

On the other hand, the studies on pure noble metal element and its binary alloy clusters have attracted considerable interest in recent years. A more recent experiment[12] did prove the presence of small binary alloy Au_NX clusters (X =Sc, Ti, V, Cr, Mn, Fe, Co, and Ni). In contrast to pure Cu and Ag clusters, small pure Au cluster is believed[13,14] to favor three-dimensional amorphous or planar configurations. While from technical viewpoint, high-symmetrical clusters sometimes are necessary as building blocks in nanostructures such as nanograin-film and nanocrystalline materials. For the unstable icosahedral Au_{12} cage (Au_{13}), doping an 3,4*d* impurity (substituting the center Au atom with an 3,4*d* impurity) may be a good way to stabilize the structure. This has been proved feasible for Mo by a recent experiment.[15]

The above research background motivates the present study. As a continuation of previous theoretical research work, we have investigated the energetics and LSMM of a single 3,4*d* impurity encapsulated in an icosahedral Au_{12} cage by employing a state-of-the-art first-principles method called density functional for molecules (DMol)[16,17] based on density functional theory (DFT).[18,19] The case of the impurity atom substituting a surface Au atom is not included in the present study. It will be seen that some 3,4*d* impurities do display very large LSMM in the icosahedral Au_{12} cage. The calculated binding energy suggests that doping an 3,4*d* element will be a feasible way to stabilize icosahedral Au_{12} cage to yield a binary alloy cluster. The LSMM and electronic structure are discussed in detail within the spin DFT scheme. As having been frequently found in many other kinds of low-dimensional systems such as surface, overlayer, sandwich, superlattice and adatom absorbed on a surface, we believe that large magnetic moment could also be found in a binary alloy cluster.

II. METHOD AND COMPUTATIONAL DETAIL

DMol is a widely used real-space first-principles cluster method, and has been successfully applied to many problems such as structural stability of molecular clusters, chemisorption and surface reconstruction. It can perform accurate and efficient self-consistent calculation and structural optimization. The equilibrium structure can be obtained by relaxing atom until the energy gradients are deemed to be zero.

To ensure the results accurate and reliable, we have chosen an exchange correlation functional proposed by Perdew (PW91),[20] a general gradient approximation (GGA) that has been successfully applied to the studies on transition metal systems, for instance, medium-size Mn clusters.[21] The rela-

TABLE I. The binding energies (BE, in eV) and equilibrium distances (r, in Å) of $3,4d$ and Au dimers obtained by using a basis set composed of double numerical basis with polarized functions.

	Theory		Experiment[a]	
	BE	r	BE	r
Ti_2	4.250	1.968	1.54±0.19	1.942
V_2	5.355	1.799	2.75	1.783
Cr_2	0.638	1.648	1.53±0.06	1.679
Mn_2	0.802	2.580	0.3±0.3	3.4
Fe_2	3.392	1.994	1.15±0.09	2.02
Ni_2	5.535	2.107	2.04	2.155
Nb_2	4.458	2.137	5.22±0.31	2.078
Mo_2	2.617	1.990	4.474±0.010	1.94
Rh_2	5.619	2.260	2.460±0.005	2.28
Au_2	2.165	2.489	2.29	2.472

[a]The experimental data can be found in Refs. 32–44.

tivistic effect is significant for Au. Currently, DMol can consider scalar relativistic effects, such as Darwin and mass velocity, by either effective core potential calculation or all-electron calculation. The properties of those heavier atoms are reproduced using an essentially nonrelativistic Hamiltonian including pseudopotentials representing scalar relativistic effects.[22–24] A basis set composed of double numerical basis ($3d,4s$ doubled for $3d$ impurity and $4d,5s$ doubled for $4d$ impurity, and $5d,6s$ doubled for Au) with polarized functions ($4p$ for $3d$ impurity and $5p$ for $4d$ impurity, and $6p$ for Au) is adopted, and all-electron spin-unrestricted calculations are performed. These can ensure much better descriptions on binding energy and magnetism, and minimize the influence of basis on calculation results to the least. The quality of the basis set was discussed in detail in the previous literatures.[16,17] We have further checked the basis set by calculations on some $3,4d$ and Au dimers. It can be seen from Table I that the present selected basis set can give reasonable results except for Mn dimer, comparable to the various different basis sets used in the recent *ab initio* studies.[25,26] Note all these theoretical studies failed in Mn dimer and have some errors on binding energy.

Figure 1 shows the geometrical structure of a single $3,4d$ impurity encapsulated in an icosahedral Au_{12} cage. In structural optimization, the 12 Au atoms are relaxed freely under I_h symmetry. The energy gradient and atomic displacement are converged to 3×10^{-3} eV Å^{-1} and 1×10^{-4} Å respectively. For self-consistent field iteration, the charge density is converged to 1×10^{-5}, which corresponds to a total energy convergence of 1×10^{-6} eV. The order of the multipolar function used for fitting charge density and solving Coulomb potential is set to be one greater than the maximum angular momentum in the basis set. About 1500 fixed integration points around each atom are used. The binding energy (BE) is defined as

$$\mathrm{BE} = E_a - E_t,$$

where E_a is the sum of the total energies of all single atoms and E_t is the total energy of the cluster.

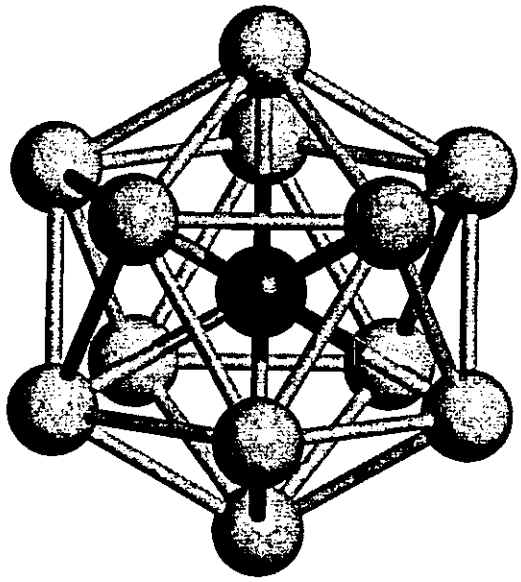

FIG. 1. The cluster model of a single $3,4d$ impurity encapsulated in an icosahedral Au_{12} cage. The center dark ball represents the $3,4d$ impurity and the outside 12 gray balls represent Au atoms.

III. RESULTS AND DISCUSSIONS

The calculated results are summarized in Table II with that on icosahedral Au_{13} for comparison. It is interesting to know if the doped icosahedral Au_{12} could be stabilized at a three-dimensional shape. This can be simply concluded by comparing the BE of doped Au_{12} with that of pure Au_{13}. As well known, energy difference between two isomers is rather significant if the value exceeds 1 eV per cluster. From Table II we can see that the BE's of the doped Au_{12} clusters are surprisingly larger than that of pure icosahedral Au_{13}. The smallest and the largest relative BE's compared with pure icosahedral Au_{13} appear at Pd and Zr, 2.186 and 7.791 eV per cluster, respectively. Clusters doped with Ti, V, and Ni also show very large relative BE's beyond 7.0 eV per cluster. The relative BE's of the rest doped clusters are beyond 3.2 eV per cluster. Even though it is not much strict to make conclusions only from BE, these unusual large relative BE's still convince us that doping a single $3,4d$ impurity could make the icosahedral Au_{12} cage stable, and form a new binary alloy cluster of three-dimensional rather than planar structure.

Local magnetism is another interesting problem in these doped systems. For $3d$ impurities Sc, Ti, and V just show small LSMM's while relatively large LSMM's are observed from Cr to Ni. Mn has the largest one, about 3.51 μ_B and then Fe about 3.06 μ_B. These features basically extend to $4d$ impurities except that all their LSMM's decrease to a certain extent and an "abnormal" case occurs to Mo. The former part of elements Y, Zr, and Nb still show small LSMM's and the latter ones from Tc to Pd show relatively strong LSMM's. Ru has the largest LSMM about 1.14 μ_B and Rh is next to it, about 0.89 μ_B. It is meaningful to know why these $3,4d$ impurities display so different LSMM's as being encapsulated in an icosahedral Au_{12} cage. We can give a simple qualitative explanation by considering the chemical bonding

TABLE II. The calculated data on a single 3,4*d* impurity encapsulated in an icosahedral Au_{12} cage: the cluster binding energy (BE, in eV), the cluster radius R (in Å), the HOMO and LUMO states (symmetry and spin), the HOMO-LUMO gap ΔE (in eV), the electron occupation number n in the HOMO, the total magnetic moment M_t of cluster (in μ_B), and the atomic magnetic moment M (in μ_B). Symbol + and − denote spin-up and spin-down states, respectively. Data on pure icosahedral Au_{13} and the relative binding energy (RBE, in eV) compared to Au_{13} are included. Some data obtained by nonrelativistic all-electron calculations are given in the parentheses for comparison.

	BE	RBE	R	HOMO	LUMO	ΔE	n	M_t	$M_{3,4d}$	M_{Au}
Sc	33.796(14.342)	5.965(4.682)	2.690(2.975)	HG(−)	AG(+)	1.973(1.315)	2	3	0.190(0.765)	0.234
Ti	35.320(15.374)	7.489(5.714)	2.659(2.943)	HG(−)	HG(+)	1.814(1.320)	3	2	0.265(1.286)	0.145
V	34.901(15.409)	7.070(5.749)	2.643(2.928)	HG(−)	HG(+)	1.241(0.982)	4	1	0.480(2.547)	0.043
Cr	31.507(12.631)	3.676(2.971)	2.642(2.925)	HG(−)	HG(+)	0.790(0.818)	5	0	2.265(3.646)	−0.189
Mn	31.061(12.526)	3.230(2.866)	2.648(2.920)	HG(+)	HG(−)	1.300(0.508)	1	1	3.512(3.785)	−0.209
Fe	32.035(13.585)	4.204(3.925)	2.643(2.908)	HG(+)	HG(−)	0.758(0.540)	2	2	3.064(2.826)	−0.089
Co	32.239(14.163)	4.408(4.503)	2.637(2.900)	HG(+)	HG(−)	0.469(0.414)	3	3	1.947(1.608)	0.088
Ni	32.009(14.321)	4.178(4.661)	2.638(2.900)	HG(+)	HG(−)	0.362(0.365)	4	4	0.943(0.665)	0.255
Y	32.934(14.366)	5.103(4.706)	2.760(3.039)	HG(−)	T2U(+)	2.116(1.579)	2	3	0.144(0.815)	0.238
Zr	35.622(16.334)	7.791(6.674)	2.722(2.996)	HG(−)	AG(+)	2.077(1.625)	3	2	0.163(0.887)	0.153
Nb	35.125(15.511)	7.294(5.851)	2.693(2.967)	HG(−)	HG(+)	2.016(1.715)	4	1	0.135(0.818)	0.072
Mo	32.675(14.442)	4.844(4.782)	2.677(2.945)	HG(±)	HG(±)	1.578(1.705)	10	0	0.000(0.000)	0.000
Tc	32.892(15.423)	5.061(5.763)	2.676(2.939)	HG(+)	HG(−)	0.242(0.233)	1	1	0.758(1.000)	0.020
Ru	31.184(14.720)	3.353(5.060)	2.678(2.938)	HG(+)	HG(−)	0.347(0.262)	2	2	1.137(0.961)	0.072
Rh	31.314(14.463)	3.483(4.803)	2.681(2.938)	HG(+)	HG(−)	0.323(0.274)	3	3	0.893(0.581)	0.176
Pd	30.017(11.790)	2.186(2.130)	2.688(2.950)	HG(+)	HG(−)	0.309(0.329)	4	4	0.460(0.233)	0.295
Au	27.831(9.660)		2.700(2.996)	HG(+)	HG(−)	0.358(0.408)	5	5	0.223(0.034)	0.398

and the magnetic interaction, two important opposite and competitive factors for BE of transition metal cluster or cluster including transition metal elements. A cluster usually tends to enhance its BE and to make the structure stable and compact by forming chemical bonds as more as possible. This, however, is not the most efficient way even the chemical bonding making the most contributions to BE. The magnetic interaction sometimes also plays an important role. To increase the exchange-splittings of *d* orbitals by reducing the strength of some chemical bonds can further enhance the BE. As a result of the competition between the two factors, a cluster finally reaches its stable structural and magnetic states. The former part of 3*d* elements such as Sc, Ti, and V show weak LSMM's because of the activities of their *s*,*p* electrons, which result in strong hybridizations that can suppress the occurrence of large exchange splittings of 3*d* orbitals, reducing the magnetic interaction. For the latter part of 3*d* elements from Cr to Ni, the magnetic interaction becomes strong enough to yield comparatively large LSMM. We can see that Cr, Mn, and Fe even make the polarization of Au_{12} cage antiparallel with their LSMM's. The relative weakness of LSMM's of 4*d* impurities is mainly related to their large atomic radii. Large overlaps between the atomic orbitals could not promote the formation of LSMM. The case of Mo seems "abnormal." The magnetic interaction is completely suppressed by the chemical bonding and all electrons are paired to give a closed-shell system. Our results on Mo are consistent with the experiment.[15] It is worthwhile to mention another similar theoretical study on an 5*d* element of same column W,[27] where a highly stable closed-shell structure of W encapsulated in an icosahedral Au_{12} cage is predicted.

Compared with the doped clusters, Au_{13} has the highest total magnetic moment. The individual Au atom in it, however, just shows small magnetic moment. The most number of unpaired electrons rather than the largest exchange-splittings result in the highest total magnetic moment of Au_{13}. Certainly a small exchange-splitting of molecular orbital is necessary in this regard. This is physically reasonable since Au is not a magnetic element. The number of paired electrons in the HOMO and its neighboring occupied molecular orbitals increases from Sc to Cr and Y to Mo, and decreases from Mn to Ni and Tc to Pd. Consequently, the total magnetic moment of cluster decreases from Sc to Cr and Y to Mo, but increases from Mn to Ni and Tc to Pd. This looks similar to the occupation feature of the "rigid band" in a alloy with different impurities. Nevertheless, we should notice that the LSMM for each individual atom in these doped clusters is not proportional to the total magnetic moment of cluster. Such case is easily seen in the spin antiparallel systems such as Cr, Mn, and Fe doped clusters. For case of Cr, the total magnetic moment of cluster is zero. The Cr impurity, however, has a rather large LSMM (2.265 μ_B).

The size effect on LSMM is always dramatic. To see this, here we draw a comparison between the LSMM in the cluster and that in the solid for all 3*d* impurities except for Sc. Compared with the nearest neighboring interatomic distances in the solid (about 2.89, 2.62, 2.50, 2.48, 2.50, and 2.49 Å for hcp Ti, bcc V, bcc Cr, bcc Fe, hcp Co, and fcc Ni, respectively), the interatomic distance between the 3*d* impurity and Au (the cluster radius shown in Table II) decreases by about 8% for Ti, but increases by about 5% for Cr, Fe, Co, and Ni, and changes slightly for V. The bulk hcp Ti and bcc V are

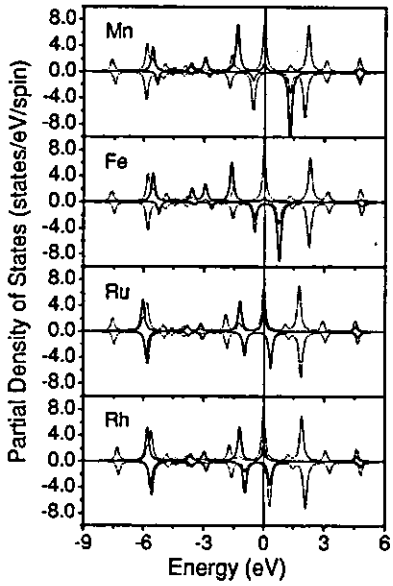

FIG. 2. The spin-dependent partial density of states for Mn, Fe, Ru, and Rh encapsulated in an icosahedral Au_{12} cage. The spin-up and the spin-down states are displayed in the up panel (plus value) and down panel (minus value), respectively. The solid line represents the *d* states of transition metal element, and the dashed line represents the *s* states of Au. Fermi level is shifted to zero.

Pauli paramagnets and hardly show any LSMM.[28] While in cluster they can have small LSMM)s, about 0.27 and 0.48 μ_B, respectively. The bcc Cr is thought to be a spin density wave system with just a small amplitude of LSMM (the maximum is about 0.60 μ_B).[28] Mn, Fe, Co, and Ni are strong magnetic elements. They can show net LSMM's at complex cubic (the maximum is about 1.90 μ_B), bcc (2.13 μ_B), hcp (1.52 μ_B), and fcc (0.57 μ_B) structures, respectively.[28,29] From Cr to Ni, obviously all their LSMM's are enhanced greatly when they are encapsulated in an icosahedral Au_{12} cage, where the increased interatomic distance plays an important role.

For system made up of transition and noble metal elements, orbital usually makes little contributions to the magnetic moment. A spin exchange-splitting picture based on spin DFT is enough to give a good description on such problem. As an illustration, we present in Fig. 2 the spin-dependent partial density of states (PDOS) for four typical transition metal elements Mn, Fe, Ru, and Rh. The PDOS is calculated by broadening the energy levels ε_i^σ of molecular orbitals (σ denote spin state) by using a line-shape function Lorentzian with width δ=0.1 eV as follows:

$$\mathrm{DOS}_{\alpha nl}^{\sigma}(E) = \sum_i P_{i,\alpha nl}^{\sigma} \frac{\delta/\pi}{(E-\varepsilon_i^{\sigma})^2 + \delta^2},$$

where $P_{i,\alpha nl}^{\sigma}$ (α denotes atom, *n* and *l* are, respectively, main and angular quantum numbers) is the state component of atomic orbital in molecular orbital (ε_i^{σ}) obtained by Mulliken analysis.[30] Obviously, strong hybridizations between the *d* orbitals of 3,4*d* impurity and the 6*s* orbital of Au occur in a wide energy range, from about −5.5 to 5.0 eV. A strong resonant peak appearing at a rather low energy site −5.5 eV

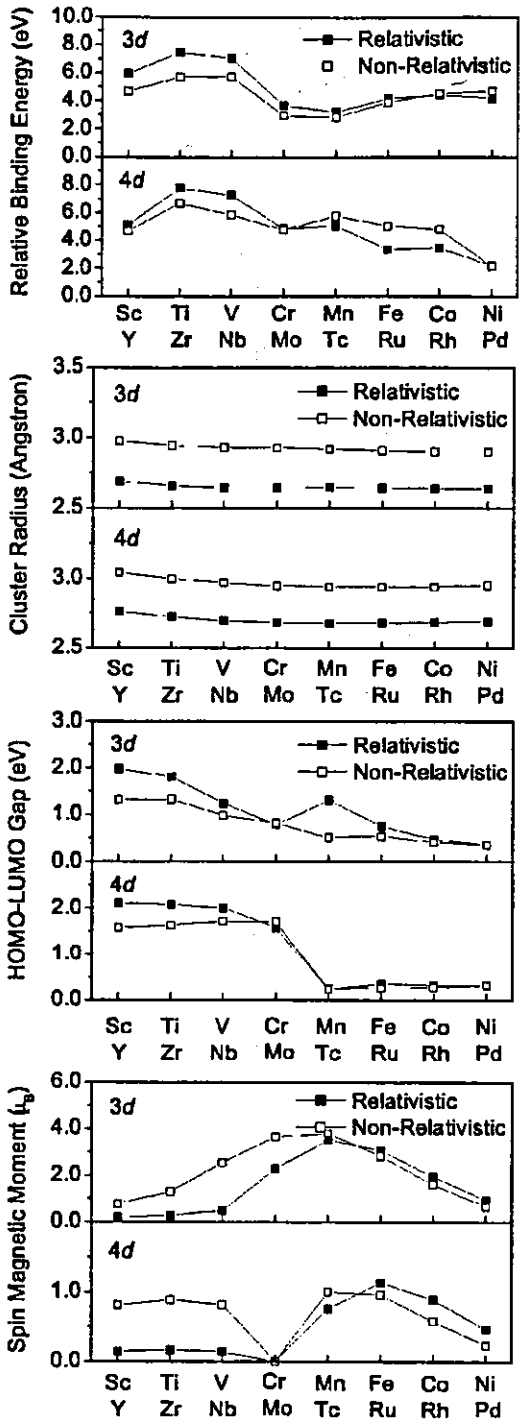

FIG. 3. The relativistic effects on the relative binding energy (compared with icosahedral Au_{13}), the cluster radius, the HOMO-LUMO gap, and the spin magnetic moment.

seems unusual since the *d* states are usually localized around the Fermi level. The *d* orbitals of Mn and Fe show larger exchange splittings than those of Ru and Rh near the Fermi level, resulting in larger magnetic moments. The *s-d* hybridizations and exchange-splittings of *d* orbitals are the main features of interaction in these doped clusters.

Relativistic effects (RE's) are particularly important for Au_{13}.[31] Table II and Fig. 3 present, respectively, the results

obtained by relativistic and non-relativistic all-electron calculations and their comparisons. The RE's corrections on the results are not so systematic but obvious. They are more significant for the former part than for the latter part of $3,4d$ impurities. The RE's correction on relative BE (compared with icosahedral Au_{13}) is remarkable for all $3,4d$ impurities except for Co, Mo, and Pd. It yields the enhanced relative BE's for the former part of $3,4d$ impurities from Sc to Cr and Y to Nb, but the weakened relative BE's for the latter part of $4d$ impurities from Tc to Rh. The bond length is rather sensitive to the RE's correction for all the doped clusters, whose structures become more compact if the RE's correction is considered. The RE's corrections on these cluster radii are close to a stable value, about 0.27 Å. The change of HOMO-LUMO gap is significant for impurities from Sc to V and Y to Nb, and also for Mn and Fe. The RE's correction gives enhanced HOMO-LUMO gaps of these impurities. The LSMM is also sensitive to RE's correction for the former part of $3,4d$ impurities from Sc to Cr and Y to Nb, whose LSMM's are weakened greatly. The LSMM's of impurities from Fe to Ni and Ru to Pd, however, are enhanced to some extent. The results for Mo seem insensitive to the RE's correction except for cluster radius.

IV. SUMMARY

Cluster method based on DFT is used to explore the energetics and local spin magnetic moment of a single $3,4d$ impurity encapsulated in an icosahedral Au_{12} cage. All doped clusters show unexpected large relative binding energies compared with icosahedral Au_{13} cluster, indicating a high possibility of forming a new binary alloy cluster. Large spin magnetic moments are observed for $3d$ impurities Cr, Mn, Fe, Co, and Ni, and $4d$ impurities Tc, Ru, and Rh due to large exchange splittings of d orbitals. Strong hybridizations between the d orbitals of $3,4d$ impurity and the $6s$ orbital of Au occur. The correction of relativistic effect is very important for electronic structure.

ACKNOWLEDGMENTS

The authors would like to express their sincere thanks to the crew of Center for Computational Materials Science of the Institute for Materials Research, Tohoku University for their continuous support of the supercomputing facilities.

*Electronic address: sywang@imr.edu

[1] D. van der Marel, C. Westra, and G. A. Sawatzky, Phys. Rev. B **31**, 1936 (1985).
[2] D. Riegel, L. Büermann, K. D. Gross, M. Luszik-Bhadra, and S. N. Mishra, Phys. Rev. Lett. **61**, 2129 (1988).
[3] N. Papanikolaou, N. Stefanou, R. Zeller, and P. H. Dederichs, Phys. Rev. B **46**, 10858 (1992).
[4] R. N. Nogueira and H. M. Petrilli, Phys. Rev. B **63**, 012405 (2000).
[5] H. Beckmann and G. Bergmann Phys. Rev. Lett. **83**, 2417 (1999).
[6] P. Gambardella, S. S. Dhesi, S. Gardonio, C. Grazioli, P. Ohresser, and C. Carbone, Phys. Rev. Lett. **88**, 047202 (2002).
[7] D. Bagayoko, N. Brener, D. Kanhere, and J. Callaway, Phys. Rev. B **36**, 9263 (1987).
[8] B. I. Dunlap, Z. Phys. D: At., Mol. Clusters **19**, 255 (1991).
[9] X. G. Gong and Vijay Kumar, Phys. Rev. B **50**, 17701 (1994).
[10] Q. Sun, X. G. Gong, Q. Q. Zheng, D. Y. Sun, and G. H. Wang, Phys. Rev. B **54**, 10896 (1996).
[11] Q. Sun, Q. Wang, J. Z. Yu, Z. Q. Li, J. T. Wang, and Y. Kawazoe, J. Phys. I **7** 1233 (1997).
[12] S. Neukermans, E. Janssens, H. Tanaka, R. E. Silverans, and P. Lievens, Phys. Rev. Lett. **90**, 033401 (2003).
[13] J. Oviedo and R. E. Palmer, J. Chem. Phys. **117**, 9548 (2002).
[14] Han Myoung Lee, Maofa Ge, B. R. Sahu, P. Tarakeshwar, and Kwang S. Kim, J. Phys. Chem. B **107**, 9994 (2003).
[15] Xi Li, Boggavarapu Kiran, Jun Li, Hua-Jin Zhai, and Lai-Sheng Wang, Angew. Chem., Int. Ed. **41**, 4786 (2002).
[16] B. Delley, J. Chem. Phys. **92**, 508 (1990).
[17] B. Delley, J. Chem. Phys. **94**, 7245 (1991).
[18] P. C. Hohenberg and W. Kohn, Phys. Rev. **136**, B864 (1964).
[19] W. Kohn and L. J. Sham, Phys. Rev. **140**, A1133 (1965).
[20] J. P. Perdew and Y. Wang, Phys. Rev. B **45**, 13244 (1992).
[21] Tina M. Briere, Marcel H. F. Sluiter, V. Kumar, and Y. Kawazoe, Phys. Rev. B **66**, 064412 (2002).
[22] B. Delley, Int. J. Quantum Chem. **69**, 423 (1998).
[23] L. F. Pacios and P. A. Christiansen, J. Chem. Phys. **82**, 2664 (1985).
[24] M. M. Hurley, L. F. Pacios, P. A. Christiansen, R. B. Ross, and W. C. Ermler, J. Chem. Phys. **84**, 6840 (1986).
[25] S. Yanagisawa, T. Tsuneda, and K. Hirao, J. Chem. Phys. **112**, 545 (2000).
[26] S. Yanagisawa, T. Tsuneda, and K. Hirao, J. Comput. Chem. **22**, 1995 (2001).
[27] Pekka Pyykkö and Nino Runeberg, Angew. Chem., Int. Ed. **41**, 2174 (2002)
[28] *Landolt-Bornstein, Numerical Data and Functional Relationships in Science and Technology*, New Series, edited by K.-H. Hellwege, and O. Madelung, *Group III: Crystal and Solid State Physics*, Vol. 19, Subvol. a (Springer-Verlag, Heidelberg, 1986).
[29] *Landolt-Bornstein, Numerical Data and Functional Relationships in Science and Technology*, New Series, Group III, Vol. 32, Supplement to Vol. 19, Subvol. A, edited by H. P. J. Wijn (Springer-Verlag, Heidelberg, 1997).
[30] R. S. Mulliken, J. Chem. Phys. **23**, 1833 (1955).
[31] P. Pyykkö, Chem. Rev. (Washington, D.C.) **88**, 563 (1988).
[32] H. Åkeby and L. G. M. Pettersson, J. Mol. Spectrosc. **159**, 17 (1993).
[33] L. M. Russon, S. A. Heidecke, M. K. Birke, J. Conceicao, M. D. Morse, and P. B. Armentrout, J. Chem. Phys. **100**, 4747 (1994).
[34] E. M. Spain, J. M. Behm, and M. D. Morse, J. Chem. Phys. **96**, 2511 (1992).
[35] B. Simard, M.-A. Lebeault-Dorget, A. Marijnissen, and J. J. ter Meulen, J. Chem. Phys. **108**, 9668 (1998).
[36] S. K. Loh, L. Lian, D. A. Hales, and P. B. Armentrout, J. Phys.